This document is the post-print version of the paper "Influence of PbLi hydraulic path and integration layout on MHD pressure losses" published on Fusion Engineering and Design. Doi: https://doi.org/10.1016/j.fusengdes.2020.111517

Influence of PbLi hydraulic path and integration layout on MHD pressure losses

Alessandro Tassone[1]*, Gianfranco Caruso[1], Alessandro Del Nevo[2]

[1] *DIAEE Nuclear Section - Sapienza University of Rome, Corso Vittorio Emanuele II, 244, 00186, Roma, Italy*

[2] *ENEA FSN-ING-PAN, ENEA CR Brasimone, 40032, Camugnano (BO), Italy*

Abstract

A critical point in the design of liquid metal blankets for fusion reactors is the accurate estimate of magnetohydrodynamic (MHD) pressure losses caused by the interaction between flowing breeder and magnetic field. In the Water-Cooled Lithium Lead (WCLL), the liquid metal (PbLi) is used as tritium breeder and carrier, whereas power extraction is delegated to water, thus allowing to minimize the breeder velocity. However, pressure drop for the PbLi loop is expected to remain significant due to high field intensity and direct electrical contact at fluid/wall interface. In this study, a comparative analysis between four alternative WCLL-DEMO configurations is performed to investigate the influence of blanket layout and piping system integration on this variable. Empyrical and semi-empyrical correlations, supported by numerical simulation results, have been used to estimate the baseline MHD loss, thus neglecting secondary contributions from viscous, inertial, and coupling effects. The larger contribution has been observed in the connection pipes, which are characterized by extensive length, high velocity, and large field gradients. Integration scheme with DEMO reactor is also a key factor, whereas breeding zone and manifold layout play secondary, albeit significant, roles in determining overall MHD loss. Adopting insulating elements in feeding and draining pipes should be carefully considered to reduce PbLi pumping requirements. Further numerical and experimental characterization of 3D MHD flow in manifolds and for coupling phenomena is vigorously suggested to reduce the uncertainty about blanket flow distribution and pressure loss estimate.

Keywords: Magnetohydrodynamics (MHD), WCLL, breeding blanket, DEMO reactor, PbLi, liquid metal technology

1. Introduction

Liquid metals containing lithium are attractive working fluids for fusion reactor blankets since they can combine the functions of coolant, tritium breeder, and carrier. However, these fluids interact strongly with the tokamak magnetic field giving arise to a wide range of magnetohydrodynamic (MHD) effects which, at the very least, alter the component performance and, at worst, can be detrimental to its stated function [1]. Among the effects triggered by the transition to a MHD flow regime, the most dramatic is a large increase in pressure loss due to the induction of resistive Lorentz forces, whereas changes affecting flow features, heat transfer, and mass transport mechanisms, even if more subtle, are no less important [2].

To minimize pressure losses and corrosion, the power extraction function is often delegated to a secondary, non electrically conductive, fluid like water or helium, in a so-called separately cooled blanket. Nevertheless, the liquid breeder must be efficiently circulated to allow tritium processing and control, thus keeping the necessity to properly understand how the MHD effects influence the blanket performances in order to optimize the component design [2, 3].

The objective of this study is to assess how the layout of the breeder circuit, both internal and external to the breeding blanket, can affect MHD pressure losses and, consequently, provide useful data to better define both the main loop and blanket design. This work has been incorporated in a wide parametric campaign launched in 2018 to improve the Water-Cooled Lithium Lead (WCLL) blanket through the analysis of four alternative configurations characterized by different approaches to integration with breeder loop, breeding zone layout, and flow distribution scheme [4].

The wide scope and available computational tool limitations have encouraged the study of the MHD loss problem through a system-level approach which focuses on the most significant phenomena to achieve a reasonably accurate first estimate and to highlight regions where further characterization is required. This methodology allows to provide a rough figure for overall MHD loss, likely to be toward the lower end rather than conservative, and to iterate toward a more accurate estimate progressively, incorporating information that will become available on MHD phenomena in later activities. For this purpose, outcome of numerical analyses carried on the WCLL blanket in the past

*Corresponding author:

Email address: alessandro.tassone@uniroma1.it (Alessandro Tassone[1])

years have been used in this study, whenever possible, to integrate empirical and semi-empirical correlations [5–10].

During the Blanket Concept Selection Exercise in 1995, a similar methodology was adopted by Reimann et al. to analyze the importance of MHD effects occurring in Dual-Coolant (DCB) and Water-Cooled (WCB) blankets [11]. More recently, system-level analyses integrated by direct simulation results have been used to estimate overall MHD loss for the Dual-Coolant Lithium Lead (DCLL) concept, both in Europe [12, 13] and United States [14, 15]. Purely numerical analyses attempting to estimate MHD losses at blanket level are scarce due to prohibitive computational cost of 3D computations and the lack of suitable system codes. Notable examples adopting this last approach are the simulation of the Indian Lithium Lead cooled Ceramic Blanket (LLCB) Test Blanket Module (TBM) performed in 2019 [16] and, based on the same concept, the coupled system code-CFD validation exercise realized by Wolfendale & Bluck [17]. Experimental campaigns on scaled down mock-ups have been performed to characterize MHD pressure loss in the Helium-Cooled Lithium Lead (HCLL) TBM under reactor-relevant magnetic field intensity [18, 19].

2. DEMO reactor and WCLL blanket

Major engineering studies on a demonstrator fusion reactor (DEMO) have been conducted in Europe since 1990s and have been coordinated since 2014 by the EUROfusion Consortium. DEMO is expected to be a "stepping stone" device between ITER, an experimental machine aimed to demonstrate high power burning plasma regimes, and a full-fledged first-of-a-kind Fusion Power Plant (FPP). Its main goals are modest electricity production (≈ 500 MWe), to achieve tritium self-sufficiency, reasonable availability (≈30%), and provide data to extrapolate toward FPP design [20].

The most recent DEMO plant concept (DEMO2017) features a baseline pulsed machine (≈2 h) with single-null water-cooled divertor to handle particle and power exhaust. The plasma-facing First Wall (FW) is protected by a thin layer made of tungsten. Reduced activation ferritic-martensitic (RAFM) Eurofer and AISI 316 steels are envisioned as structural materials, respectively, for in-vessel components and Vacuum Vessel (VV). Magnet system provides up to 12 T and relies on Low Temperature Super Conducting Nb_3Sn magnets divided into a Central Solenoid (CS), sixteen Toroidal Field Coils (TFC), and six Poloidal Field Coils (PFC) [20].

One of the critical components to achieve DEMO goals is the Breeding Blanket (BB) which is tasked with tritium breeding, fusion power extraction, and radiation shielding. The vacuum chamber is completely surrounded by the BB which is divided in inboard and outboard sections, as shown in Figure 1. A comprehensive review on the R&D activities required for this component is presented in Ref. [1]. Currently, two different concepts are intensely pursued within EUROfusion: the Helium-Cooled Pebble Bed (HCPB) and Water-Cooled Lithium Lead (WCLL) [21].

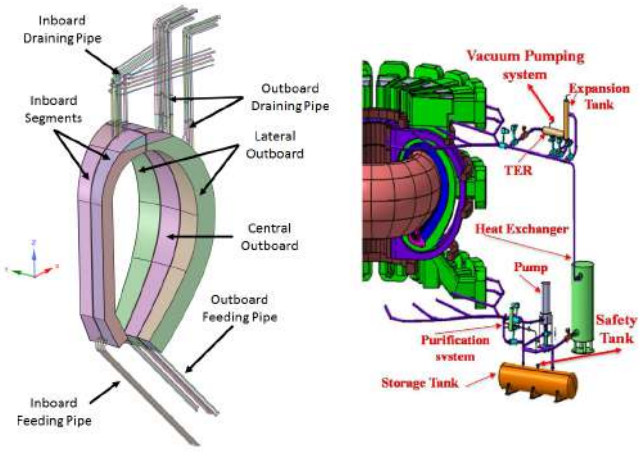

Figure 1: Blanket sector and integration with PbLi loop (shown on right, from Ref. [4]) and Primary Heat Transfer System (PHTS, not labeled), labels for the PbLi connecting pipes refer to the integration scheme no. 1 described in Section 4.2

2.1. WCLL blanket

This blanket concept relies on Lithium Lead eutectic alloy (PbLi) as tritium breeder and carrier, wheres FW and BB cooling is accomplished using pressurized water. Development activities have been performed by ENEA CR Brasimone and several institutions since 2014 [4, 22–24]. The baseline design is described in detail in Ref. [24].

PWR-like conditions ($P = 15.5$ MPa, T =295÷328 °C) are adopted for the Primary Heat Transfer System (PHTS) to draw upon abundant operative experience accumulated by fission reactors. Separate circuits are adopted for FW and BB Breeding Zone (BZ); the former relies on square channels embedded in the structural material, whereas the latter is constituted by a large number of Double-Walled Tubes (DWT) directly immersed in the breeder [4, 24].

No poloidal segmentation is considered in the current design iteration to facilitate PbLi loading/draining operations, helium bubbles removal, and radiation shielding. The BZ geometry is modular with horizontal and vertical stiffening plates (SP) identifying an "elementary cell" which represents the PbLi hydraulic path and is uniformly repeated along the poloidal direction [4, 24].

The back supporting structure (BSS) sustains the weight of the blanket segment and provides the connection with the VV. Due to the intense loads that it needs to withstand, the BSS is the thickest structural component in the blanket at ≈100 mm [4]. Water and PbLi manifolds are integrated within the narrow gap separating BSS and BZ [4, 24].

2.2. PbLi loop

The conceptual design of the PbLi loop is shown in Figure 1. Its main purpose is to circulate the liquid metal through the blanket to ensure continuous tritium removal

Table 1: Average BZ dimensionless group values in WCLL alternative configurations, described in Section 4and Table 2, and DCLL (from Ref. [27])

	Ha	Re	N	Gr	Ly
DCLL	8.05×10^3	3.18×10^4	2.00×10^3	3.73×10^{11}	1.06×10^2
WCLL					
T01.A	9.39×10^3	1.96×10^2	4.52×10^5	1.46×10^{13}	2.31×10^1
T01.B	9.39×10^3	9.78×10^3	9.04×10^3	1.46×10^{13}	2.31×10^1
T02	6.73×10^3	3.17×10^3	1.43×10^4	2.23×10^{10}	3.04×10^2
T03	6.73×10^3	7.13×10^3	6.36×10^3	2.23×10^{10}	3.04×10^2

and to minimize permeation in the primary coolant. It is divided in separately managed inboard and outboard circuits for a total of six operative loops. The liquid metal is circulated through mechanical pumps and, after passing within the blanket, is sent to the Tritium Extraction and Removal System (TER). An expansion (or relief) tank is present at the circuit top to allow helium degassing and, together with an heat exchanger and purification system, to provide chemical and volume control. Operative loop pressure is foreseen at 0.33 MPa, whereas the value for the conceptual design of components is fixed at 4.6 MPa, 110% of maximum pressure value accounting for PbLi hydrostatic load, cover gas pressure and pumping system [3, 25]. However, the design pressure is likely to be revised in the next DEMO iterations, since it currently neglects both MHD losses and peak transient value in accidental conditions, where the liquid metal can reach up to 15 MPa during in-box Loss of Coolant Accident [26]. A more realistic value for the loop design could be defined from the nominal pressure in the PHTS ($P_1 = 15.5$ MPa) through the relation

$$P_{\text{loop}} = P_1 * 1.1 + P_2 = 20.5\text{MPa} \tag{1}$$

where $P_2 = 3$ MPa is the PbLi hydrostatic load.

3. Fundamental MHD phenomena

The motion of an incompressible electrically conducting fluid in the presence of a magnetic field within a duct is fully described by the combination of Navier-Stokes and Maxwell equation sets. For liquid metal flows in fusion reactor, the induction-less approximation can be used to neglect the self-induced magnetic field effect and to simplify the velocity/magnetic field coupling [28, 29]. Focusing our attention on the momentum equation, it can be expressed as following

$$\frac{\partial \mathbf{v}}{\partial t} + (\mathbf{v} \cdot \nabla)\mathbf{v} = -\frac{1}{\rho}\nabla p + \nu \nabla^2 \mathbf{v} + \frac{1}{\rho}\mathbf{j} \times \mathbf{B} + \mathbf{f} \tag{2}$$

where $\mathbf{v}$, t, ρ, p, ν, $\mathbf{j}$, $\mathbf{B}$ and $\mathbf{f}$ stand for velocity, time, density, pressure, kinematic viscosity, current density, magnetic field, and a generic volumetric body force.

Suitable scales can be chosen, such as magnetic field intensity B_0 and characteristic length L, to rearrange Equation (2) in dimensionless form, thus defining fundamental parameter groups. The most important is the *Hartmann number*

$$Ha = B_0 L \left(\frac{\sigma}{\rho\nu}\right)^{0.5} \tag{3}$$

where σ is the electrical conductivity. This dimensionless group represents the square of electromagnetic and viscous forces ratio. The *Reynolds number* is expressed through its classic formulation

$$Re = \frac{u_0 L}{\nu} \tag{4}$$

These two parameters can be combined to write the *interaction parameter* or *Stuart number* to express the ratio between electromagnetic and inertial forces

$$N = \frac{Ha^2}{Re} = \frac{\sigma B_0^2 L}{\rho u_0} \tag{5}$$

Since intense temperature gradients are foreseen in the blanket due to neutronic volumetric heating (Q), the term f generally stands for the buoyancy force. The *Grashof number* is used to describe the ratio between buoyancy and viscous forces

$$Gr = \frac{g\beta\Delta T L^3}{\nu^2} \tag{6}$$

where g, β, and ΔT are the gravity acceleration, thermal expansion coefficient and characteristic temperature difference. Consequently, the *Lykoudis number* characterize the balance between electromagnetic and buoyancy forces

$$Ly = \frac{Ha^2}{Gr^{0.5}} \tag{7}$$

If the discussion is restricted to buoyancy as the only additional body force, Equation (2) can be reformulated to highlight the influence of these dimensionless groups

$$Ly^{-2}\left[\frac{\partial \mathbf{v}}{\partial t} + (\mathbf{v} \cdot \nabla)\mathbf{v}\right] = - \nabla p_d + Ha^{-2}\nabla^2 \mathbf{v} + \mathbf{j} \times \mathbf{B} - \mathbf{g}T \tag{8}$$

where p_d stands for the dynamic pressure. In a purely isothermal magneto-hydraulic flow, N^{-1} is substitutes to Ly^{-2} in the left hand side of Equation (8) and the buoyancy force term is omitted.

A comprehensive review of design issues introduced by the transition to MHD flow regime is outside of the scope of this study but can be found in Ref. [2]. In the present work, the focus is on the enhanced pressure loss caused by the retarding action of volumetric Lorentz forces in the fluid. These are generated by the current induction in the fluid body due to the relative movement between the electrically conducting fluid and "static" magnetic field. Ensuing Lorentz forces destroy the kinetic energy of the flow via Joule dissipation and, thus, force the fluid to rearrange its structure to minimize it. The most well-known effect is flow diffusion along magnetic field lines

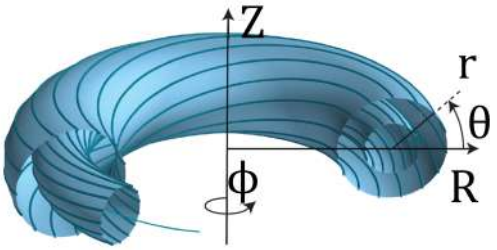

Figure 2: Quasi-toroidal coordinate system: toroidal (ϕ or t), poloidal (θ or p), vertical (Z), global (R) and blanket (r) radial axes [10]

which results in the typical "quasi-slug" core flow and dampening of turbulent structures [28, 29]. If the duct walls are electrically conductive, these provide additional current paths and their relative conductivity with regard to the liquid metal is expressed through the *wall conductance ratio*

$$c = \frac{\sigma_w}{\sigma}\frac{t_w}{L} \tag{9}$$

where σ_w and t_w are the wall electrical conductivity and thickness. Current path in the fluid bulk are mainly within thin boundary layers, whose scale is expressed as $\delta_H = \mathcal{O}(Ha^{-1})$ for wall $\perp$ **B** and $\delta_S = \mathcal{O}(Ha^{-1/2})$ for wall $\parallel$ **B**. If the magnetic field is large enough, all the current is carried by the wall and main force balance in duct is between pressure and Lorentz force, therefore $\partial p/\partial x \propto u_0 B_0^2$. However, MHD pressure loss is influenced also by other parameters, one of the most important being the channel aspect ratio.

Typical values in the WCLL for fundamental dimensionless groups are summarized in Table 1 and compared with those for Dual Coolant Breeding Blanket (DCLL) [27]. MHD flow in WCLL is mostly expected to be inertia-less and laminar with only a moderate contribution from buoyancy effects, which is mainly important for heat and mass transport phenomena but can be neglected for pressure loss evaluation.

4. Geometry definition

The PbLi loop described in Section 2.2 and its hydraulic path within the blanket can be divided into two main sections: an external or *ex-magnet* one, where the magnetic field is negligible and pressure losses are mainly due to viscous drag, and an internal or *in-magnet* section, where field intensity and MHD effects are significant. It is difficult to give an accurate definition of the boundary between these two loop sections, since the poloidal magnetic field can extend quite far into the tokamak building depending on the reactor parameters and coil arrangement. To evaluate the MHD pressure losses, it is assumed that the magnetic field influence does not extend any further than the pipes connecting each blanket segment and the PbLi main loop, whose general layout is shown in Figure 1.

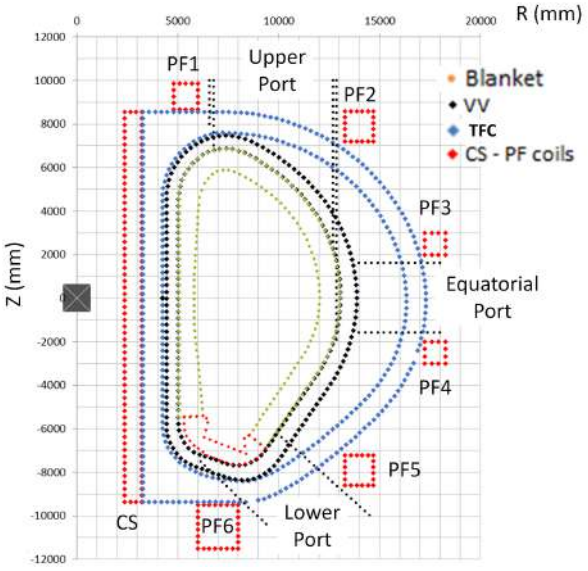

Figure 3: Global DEMO2017 layout with highlighted the position in the reactor of blanket, VV, and magnetic field coils [10]

The traditional quasi-toroidal coordinate system, as shown in Figure 2, is used to define the position of an arbitrary point in the tokamak. The blanket is divided into 16 sectors, each one covering about 22.5 ° around the torus and further divided into 2 inboard and 3 outboard segments. The analysis is focused on the central outboard segment (see Figure 1) for the most recent DEMO baseline (DEMO2017), which general layout is presented in Figure 3. The radial depth allocated for the blanket is equal to 1 m, whereas the toroidal width of the central segment is ≈ 1.5 m. PbLi loading and unloading is performed through the upper port, whereas an alternative feeding scheme, akin to the one foreseen for the inboard, is envisioned from the lower port.

The in-magnet part of the PbLi loop, i.e. blanket and connecting pipes, is divided into four main hydraulic regions:

1. **Feeding pipe (FP)**: connection pipe between PbLi ex-magnet loop and blanket
2. **Manifold (M)**: PbLi distribution and collection to/from the blanket BZ. It is composed by three sub-regions: Distribution Manifold (DM), Collection Manifold (CM), and Spinal Manifold (SM, only for T01.A)
3. **Breeding zone (BZ)**: bulk of the blanket volume dedicated to tritium production
4. **Draining pipe (DP)**: connection pipe between blanket and PbLi ex-magnet loop

The FP and DP layout is common to all the blanket configurations considered, whereas M and BZ design can vary significantly. It should be noted that, in the current iteration, only the BZ region has seen detailed work in the past, whereas the rest of the PbLi in-magnet loop is still in the early conceptual phase.

Table 2: Breeding zone and manifold general features

	T01.A	T01.B	T02	T03
		Breeding Zone		
Flow path	Radial	Radial-poloidal	Poloidal ⇑	Poloidal ⇓ / ⇑
Velocity ($mm\,s^{-1}$)	< 1	10	2	4
Length (m)	1	> 50	15	30
Pipe layout	C-pipes	C-pipes	U-pipes	Vertical
		Manifold		
Layout	Spinal	Compact	Honeycomb	Plenum
Velocity ($cm\,s^{-1}$)		$1 \div 15$	$0.5 \div 2$	$0.2 \div 1$
Length (m)	20	0.5	≈ 0.75	≈ 0.65

4.1. Blanket geometry

Four blanket configurations, whose general features are listed in Table 2, are considered to investigate its influence on the overall MHD pressure drop. Configuration T01.A (Figures 4 and 5) is the reference layout described in Refs. [23, 24, 32] which relies on very low PbLi velocity in the BZ to minimize pressure losses and a mostly radial flow path. Distribution is ensured by a manifold composed by two stacked rectangular channel arrays, which are elongated for the entire segment poloidal height and wedged in-between the blanket back plate and BSS.

Configuration T01.B (Figures 4 and 6) simplifies the manifold structure by removing the poloidal arrays and focusing flow distribution into two compact collectors localized at the segment extremities. BZ cells are interconnected at the back to allow for the liquid metal to wind through in a radial-poloidal fashion within enlarged elementary channels [33]. Nevertheless, BZ mean velocity and flow length are greatly increased.

In Configuration T02 and T03, horizontal SPs are removed in favor to a beer-box arrangement composed by toroidal-poloidal and radial-poloidal ribs [30]. Consequently, BZ elementary cells are found within poloidal channels.

Configuration T02 (Figures 7 and 8) is designed with a once-through layout, where the PbLi rises upward and is refrigerated by horizontal U-pipes [31]. Manifolds are directly integrated in the BZ with flow distribution performed either by dedicated upper and lower plena or, if the SP arrangement must be preserved to ensure the caps mechanical stability, by opportunely drilled orifices in the so-called "honeycomb" structure [10].

Finally, configuration T03 (Figures 7 and 9) is inspired to the water-cooled blanket developed in the 90s at CEA [11]. The liquid metal flows downward in the blanket back and upward in channels close to the FW. Vertical pipes ensure the breeding refrigeration [31]. Distribution and collection are localized at the blanket top where two separate plena are envisioned.

4.2. Connection pipe routing

Several routing schemes are possible to design the connection pipes tasked to link blanket and PbLi loop. Integration between in-vessel and ex-vessel system in the blanket area is foreseen through the lower and upper VV ports, which are shown in Figure 3. Three possible pipe layout are shown in Figure 10

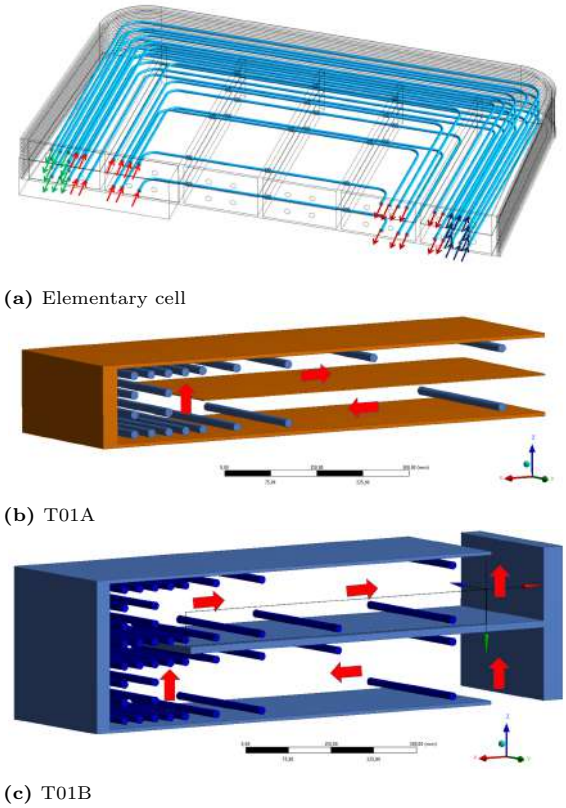

(a) Elementary cell

(b) T01A

(c) T01B

Figure 4: Breeding zone elementary cell (top, from Ref. [24]) and PbLi flow path, marked by red arrows, for configuration T01.A (middle) and T01.B (bottom)

- For the **Bottom** scheme, the pipe is routed through the lower port and connected at the blanket lowest point
- In the **Mid-level** scheme, the pipe is routed through the upper port and attached at $\approx 2/3$ of blanket height
- For the **Top** scheme, the pipe is routed in a similar way but it is connected at the blanket topmost point

The integration scheme (IS) is defined by the combination of feeding and draining pipe layout. In this study, five integration schemes are considered for the outboard blanket segment

- **IS No. 1**: Bottom (FP)–Mid-level (DP)
- **IS No. 2**: Bottom (FP)–Top (DP)
- **IS No. 3**: Mid-level (FP)–Mid-level (DP)
- **IS No. 4**: Top (FP)–Top (DP)
- **IS No. 5**: Mid-level (FP)–Top (DP)

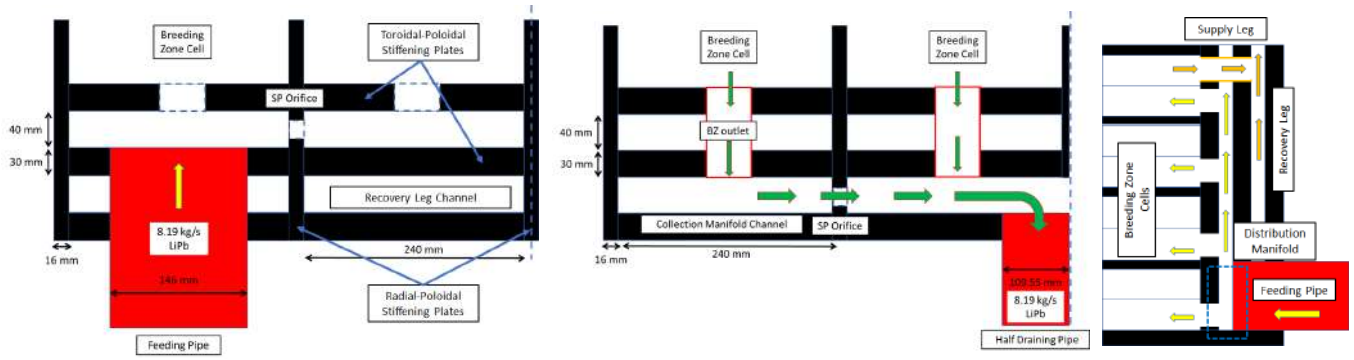

Figure 5: Manifold for configuration T01.A: distribution (left, $t-r$ view), collection (middle, $t-r$ view), and spinal ($p-r$ view) collectors

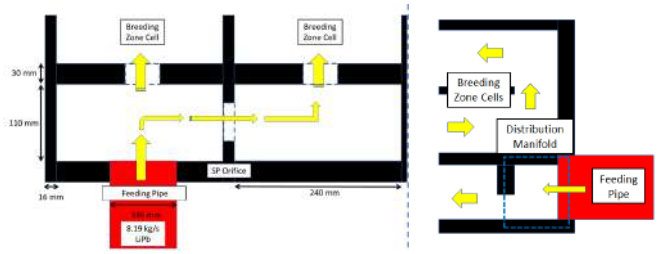

Figure 6: Manifold for configuration T01.B: distribution collector, $t-r$ (left) and $p-r$ view (right), dashed line is symmetry axis

Integration scheme no. 1 (shown in Figure 1) and no. 3 are currently the reference and backup solution for PbLi loop integration. Scheme no. 2 is inspired to the reference layout considered for inboard segment, whereas scheme no. 4 allows optimal feeding and draining from configuration T03.

5. Methodology

In this section, the methodology used for pressure loss evaluation is described. Appropriate boundary conditions for the magnetic field and interface with PbLi loop are extracted from the most recent design data.

5.1. Magnetic field

Magnetic field data in DEMO2017 are extracted from the report by Wenninger et al. [34]. In this study, the magnetic field distribution is assumed to be constant in time and equal to the calculated one in Start-of-Flat-Top (SOF) equilibrium, i.e. ramp-up phase end.

The toroidal field component is dominant and it is assumed that $B \approx B_\mathrm{t}$ for pressure drop computation for all but toroidally aligned flows in the region delimited by the internal toroidal field coil surface. At the reference radial coordinate $R_0 = 8.9316$ m, the magnetic field has the intensity $B_\mathrm{t}(R_0) = 4.8935$ T [34], whereas elsewhere $B_\mathrm{t}(R) = B_\mathrm{t}(R_0) \cdot R_0/R$. Under these conditions, the toroidal field in the blanket can vary in the range $B_\mathrm{t} = 3.35 \div 5.45$ T: the minimum is found on the equatorial plane ($Z = 0$ m), whereas the maximum is located on the top at inboard/outboard interface.

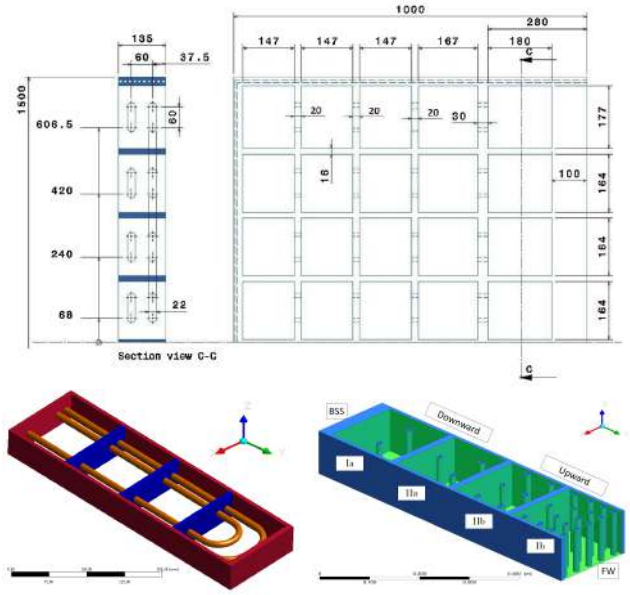

(a) T02 **(b)** T03

Figure 7: Breeding zone SP arrangement (top, $t-r$ view, from Ref. [30]) and cooling system layout (bottom) for configuration T02 and T03 (from Ref. [31])

Inside the TFC thickness, the toroidal field component decreases as $1/R$ and in the region external to the coil $B_\mathrm{t} = 0$ T, therefore the poloidal component (B_p) is used to determine the pressure losses in this region. Commonly, it is expressed through its projections on the radial (B_r) and vertical axis (B_v). The poloidal field topology is complex since it is the result of the interaction among the field produced by six PFCs and CS. An overview of typical poloidal and toroidal field values can be found in Table 3.

5.2. Boundary conditions and properties

The boundary conditions at the interface between in-magnet and ex-magnet PbLi loop are obtained from the operative conditions reported by Utili et al. for the preliminary design [3, 25].

The liquid metal is assumed to be isothermal within the entire in-magnet PbLi loop at the average operative

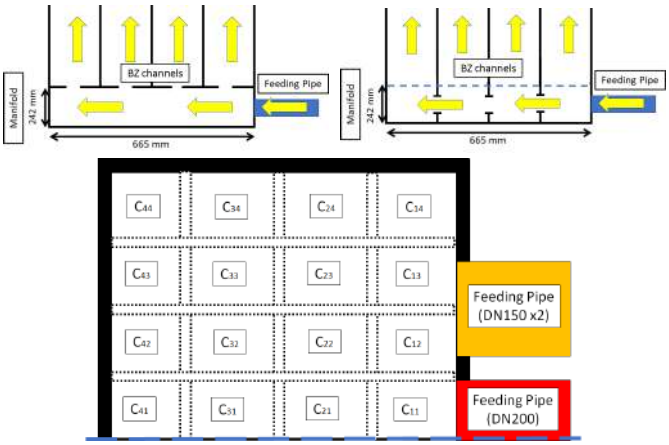

Figure 8: Manifold for configuration T02: (top) plenum and honeycomb layout in $p-r$ view, (bottom) sketch in $t-r$ view. Dashed rectangles mark SP position above (plenum) or within the manifold. SPs orifices are omitted

Table 3: Magnetic field data in DEMO2017 from Ref. [34] for several outboard blanket locations. Symbol † identifies average value, ‡ maximum value on subset $\aleph$ = [R, Z] = [(8, 15.3), (6.8, 10)] and $\Re$ = [(9.8, 15.3), (-7, -10)] (unit in m), α inclination on toroidal

	(R, Z) (m)	B_t(T)	B_p(T)	B_r(T)	B_v(T)	α(°)
FW	(8.083, 5.676)	5.407	0.349	0.292	-0.191	
BSS	(8.008, 6.758)	5.458	0.400	0.106	-0.386	
Top†		5.433	0.374			3.923
FW	(12.047, 0)	3.628	1.294	-0.011	-1.294	
BSS	(13.047, 0)	3.350	1.109	0.021	-1.109	
EOP†		3.489	1.202			18.905
FW	(8.571, -6.3)	5.099	0.530	0.079	-0.524	
BSS	(9.38, -6.888)	4.660	0.834	0.127	-0.825	
Bottom†		4.879	0.682			7.917
Complete FW†		4.187				
Complete BSS†		3.911				
Upper Port‡$\aleph$		0.000	0.909	0.314	0.483	
Lower Port‡$\Re$		0.000	1.400			

temperature $T_{\text{ref}} = 601$ K, so that physical properties can be assumed as constant. The same holds true for Eurofer. Properties are collected in Table 4.

PbLi mass flow rate at the interface is fixed to provide a complete recycle of the BB volume about 10 times per day. Under this assumption, the mass flow rate for each outboard and inboard blanket segment is, respectively, 16.38 kg s^{-1} and 5.32 kg s^{-1} [3].

Remote maintenance requirements on nominal diameter and wall thickness are taken into account to define the connection pipe geometry: currently, $80 \leq \text{DN} \leq 200$ and

Table 4: Physical properties of PbLi [35] and Eurofer steel [36] at $T_{\text{ref}} = 601$ K

Property (unit)	Symbol	PbLi	Eurofer
Density (kg m^{-3})	ρ	9.806×10^3	
Electrical conductivity (S m^{-1})	σ	7.818×10^5	1.145×10^6
Dynamic viscosity (Pa s)	μ	1.921×10^{-3}	
Magnetic permeability (H m^{-1})		μ_0	μ_0

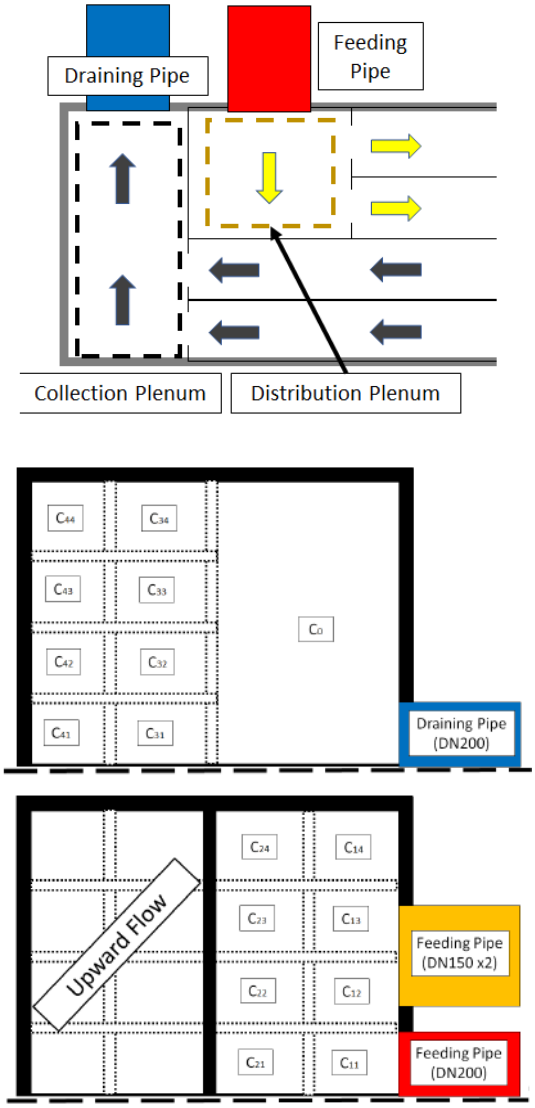

Figure 9: Manifold for configuration T02: (top) plena layout in $p-r$ view, sketch in $t-r$ view for collection (middle) and distribution (bottom) plenum. Dashed rectangles mark SP position

5 mm $\leq t_w \leq$ 15 mm. Design conditions equals to $P = 5$ MPa and T_{ref} are used to calculate the pipe thickness

$$t_w = s_f \frac{PD_o}{2S} \tag{10}$$

where D_o, $S = 100$ MPa, and $s_f = 2$ are the pipe outer diameter, maximum allowable stress, and safety factor. Loop pipes designed under these assumptions have roughly the same wall thickness than the ones designed according to Ref. [37] for internal pressure $P^{'} = 20.5$ MPa, therefore they can be considered as relatively realistic, since $P^{'}$ accounts for both peak pressure during in-box LOCA transient and PbLi hydrostatic load.

5.3. Pressure drop evaluation

If $Ha \gg 1$, the main force balance in a forced convection MHD flow is between the driving pressure gradient and

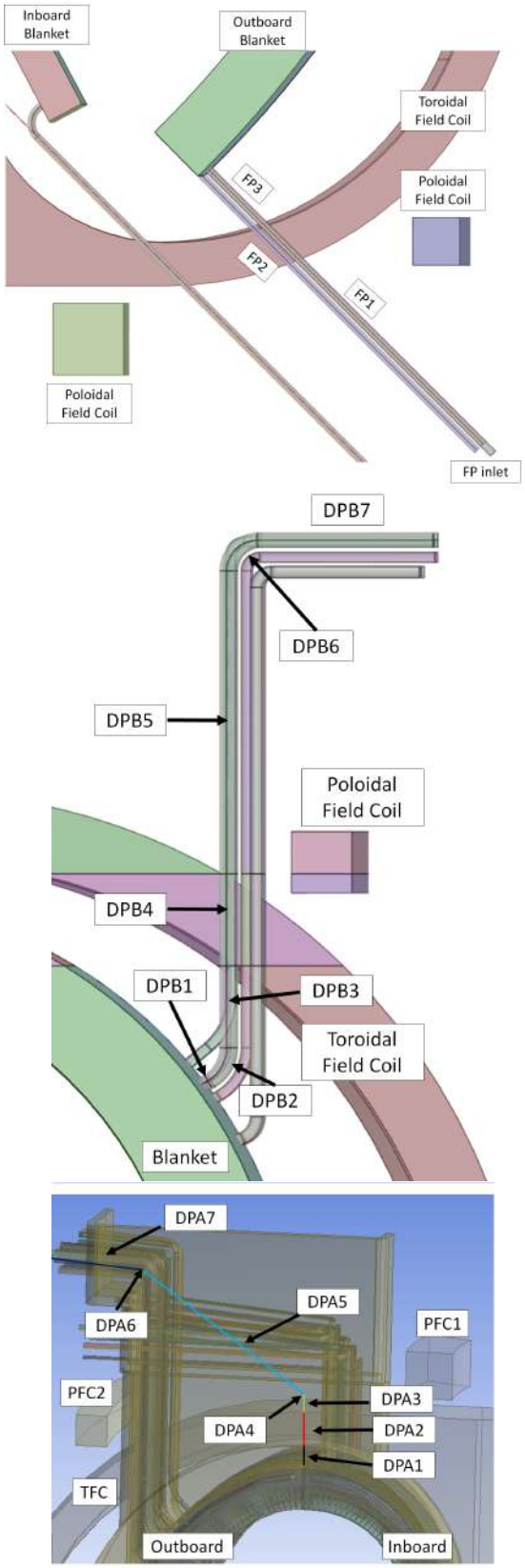

Figure 10: Blanket/Loop connection pipe routing layout: through VV lower port (top) and upper port, mid-level (middle) and top attachment

Lorentz force with viscous forces restricting their action in thin boundary layers [29]. Therefore, it is possible to neglect the ordinary hydrodynamic head loss due to friction and the overall pressure drop can be expressed as

$$\Delta p \approx \Delta p_{\mathrm{MHD}} = \Delta p_{\mathrm{2D}} + \Delta p_{\mathrm{3D}} \tag{11}$$

In Equation (11), the Δp_{2D} term is the MHD analogue of the hydrodynamic friction loss, which is caused by the cross-sectional currents induced by the relative motion between fluid and magnetic field, and can be described as an "electromagnetic drag" that dissipates the kinetic energy of the fluid through the Joule effect.

Conversely, the Δp_{3D} term is characteristic of 3D MHD flow where stream-wise velocity gradients causes the induction of additional currents, which close mostly in the fluid body, and can be considered the MHD analogue of hydrodynamic concentrated losses. Sometime this term is split in three separate contributions [38]

$$\Delta p_{\mathrm{3D}} = \Delta p_{\infty} + \Delta p_{v} + \Delta p_{i} \tag{12}$$

The first term on the right side, mainly due to electromagnetic forces, is called inertia-less/inviscid and, for $Ha \gg 1$ and $N \gg 1$, Equation (12) reduces to $\Delta p_{\mathrm{3D}} \approx \Delta p_{\infty}$. The second and third term are caused by, respectively, viscous and inertial forces. These terms are not expected to play a significant role in the WCLL due to low fluid velocity and high magnetic field intensity. However, the inertial term could be non-negligible in manifolds and feeding/draining pipes, thus requiring the adoption of conservative assumptions.

It should be noted that Equation (11) implicitly makes the assumption that 2D and 3D pressure drop terms can be easily distinguished for an arbitrary flow path, which does not always hold true in practice. Moreover, it implies that only currents induced within the fluid body contributes to the pressure losses. This hypothesis well represents the flow in a duct immersed in a dielectric medium, i.e. air, which is typical in experimental conditions, but neglects the effect of leakage currents penetrating from nearby ducts that are in electrical contact, often encountered in blankets [39]. Electromagnetically coupled channels behave differently than uncoupled ones experiencing, among other effects, global flow rearrangement and modified pressure loss trends [40–45]. In this study, such effects and their impact on the global pressure loss are neglected. Some basic considerations are provided in Sections 7 and 8, but a more detailed analysis should take into account these phenomena.

Maximum allowable MHD loss for both inboard and outboard blanket loop is usually considered equal to 2 MPa [2]. However, this figure should be seen more as a rule of thumb value rather than a fixed design limit, even if it is considered as reliable guideline for the purpose of this study. A more rational definition of the maximum allowable limit should be formulated after a careful assessment taking into account the technological limitations for the manufacturing

of liquid metal pumping systems. Secondarily, DEMO power available to satisfy PbLi pumping requirements and pressure stresses sustainable by structural elements in the most demanding scenario, for instance in-box LOCA with "warm" blanket, should be considered.

5.3.1. 2D pressure losses

Most of the PbLi hydraulic path in the WCLL blanket can be approximated by straight channels with constant cross-section where, thanks to the high magnetic field intensity, the flow is in fully developed state, so that $\Delta p \approx \Delta p_{2D}$. Assuming the magnetic field to be uniform, uni-directional and transverse to the flow, the head loss can be calculated straightforwardly from the following relation for the pressure gradient

$$\partial p/\partial x = k_p \sigma u_0 B_0^2 \tag{13}$$

where the value of pressure coefficient k_p is influenced by the channel cross-section type, geometry and wall conductivity. If $Ha \gg 1$, this parameter is defined such as $k_p = c/(1 + c + a/3b)$ or $k_p = c/(1 + c)$ for a duct with uniform wall conductance ratio and, respectively, rectangular or circular cross-section [46–48]. For a duct with non-uniform wall conductance ratio, which it is a common case in the blanket, the expression $k_p = [1 + c_H^{-1} + a/6b(c_{S,1}^{-1} + c_{S,2}^{-1})]^{-1}$ is used that, however, is valid only for a rectangular channel with uniform Hartmann wall conductivity (c_H) [49]. For duct geometries that cannot be treated with this last relation, the wall with highest conductive ratio is assumed to be representative for the whole channel and the relation for uniform wall conductivity is applied.

Several authors have compared predictions obtained with Equation (13) against the effective pressure gradients observed experimentally [46, 50–56]. An overview of the deviation between theoretical and averaged measured pressure coefficient k_p is given in Table 5 and graphically presented in Figure 11. The straight duct MHD flow is well characterized and pressure loss can be estimated with relatively good confidence, i.e. ±15%.

In Section 5.1, it was discussed how the toroidal magnetic field is dominant in the blanket but, even neglecting the poloidal component, it is far from being completely consistent with the unidirectional assumption. In particular, small misalignment between blanket wall and magnetic field is expected due to toroidal segmentation [11, 57] which, in the present case, can be estimated for the outboard as $\gamma = 180/(n/2 \cdot 3) = 7.5^\circ$, where $n = 16$ is the blanket sector number. Even if it can cause side layer detachment from the wall for poloidal flows, this phenomenon is not expected to cause significant losses enhancement and it is neglected [11, 58].

On the other hand, the poloidal component cannot be neglected when considering radially oriented flows, especially if the duct is characterized by large aspect ratio. On the equatorial plane, an inclination of about 19° from toroidal plane is observed with misalignment decreasing toward blanket extremities [5, 11, 57]. As suggested by Kirillov et al.[46], a correction factor $\lambda(\alpha) = 1.7$ is employed to model the field misalignment effect on the pressure losses for radial 2D MHD flow on equatorial plane, which is consistent with the results reported by Hua & Walker for $a/b = 2$ [10, 59].

Table 5: Average measured (k_{exp}) versus calculated (k_{th}) 2D MHD pressure coefficient for rectangular and circular channels

Cross-section	$k_{\text{exp}} \cdot 10^3$	$k_{\text{th}} \cdot 10^3$	Δk (%)	Ref.
Rectangular	3.97	4.37	10.076	[50]
Circular	4.72	3.88	−17.797	[46]
Rectangular	22.30	21.00	−5.830	[46]
Circular	24.60	25.30	2.846	[46]
Rectangular	26.50	25.90	−2.264	[46]
Rectangular	28.70	27.80	−3.136	[46]
Circular	37.80	35.10	−7.143	[46]
Rectangular	38.74	36.35	−6.169	[52]
Circular	40.00	38.50	−3.750	[46]
Rectangular	40.24	36.35	−9.667	[52]
Circular	48.63	45.80	−5.821	[51]
Rectangular	52.40	51.90	−0.954	[46]
Circular	56.10	56.60	0.891	[46]
Rectangular	61.60	61.60	0.000	[46]
Circular	64.50	64.50	0.000	[46]
Circular	67.34	67.80	0.683	[56]
Rectangular	72.00	81.90	13.750	[46]
Rectangular	78.50	69.5	−11.465	[55]
Circular	80.70	76.60	−5.081	[46]
Rectangular	97.89	95.97	−1.961	[50]
Circular	159.87	156.02	−2.408	[53]
Rectangular	232	249.25	7.435	[54]
Rectangular	266	256	−3.759	[54]

5.3.2. 3D pressure losses

Three-dimensional MHD flows are less characterized than fully developed flows and, correspondingly, the pressure losses evaluation is much more complicated due to being strongly dependent on the case geometry and governing parameters. In this study, 3D MHD flows are assumed to be locally inertia-less and inviscid so that $\Delta p_{3D} = \Delta p_\infty$ in Equation (11). However, inertial effects could be observed in complex geometries where high velocity are expected, like in the manifold, affecting both losses and velocity distribution. Insufficient information is currently available for their estimation and conservative assumptions on the magnetic field intensity are used to partially account for their influence.

Three-dimensional pressure drop is evaluated with the classic relation [2]

$$\Delta p_{3\text{D}} = \frac{1}{2} k_{3\text{D}} \rho u_0^2 N \tag{14}$$

with $k_{3\text{D}}$ and N being the 3D pressure coefficient and local interaction parameter, which is calculated adopting $L_{3\text{D}}$ as length scale, usually the channel half-width in magnetic field direction. The value of 3D pressure coefficient is strongly dependent on the local geometry and flow parameters.

Bends. Three-dimensional MHD flow in bends have been studied experimentally [60–64], via asymptotic analyses

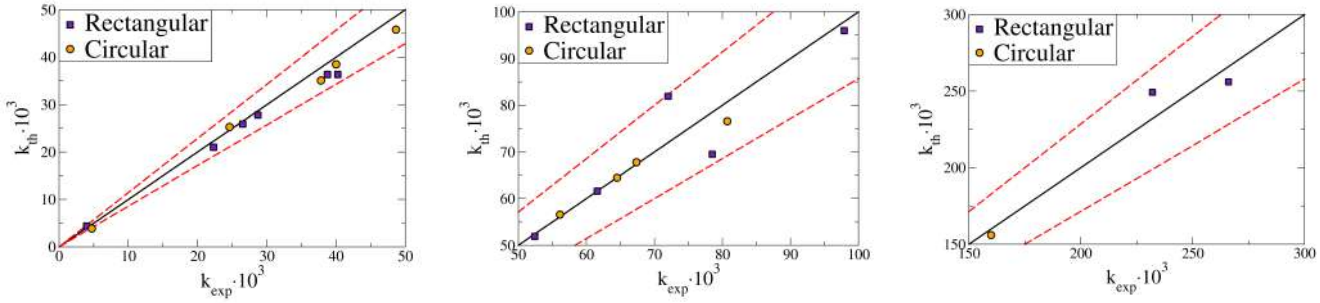

Figure 11: Relative error between theoretical and experimental pressure coefficient k_p for rectangular and circular ducts. Dashed lines identify a relative error equal to ±15%. The data presented in these plots are collected in Table 5.

[65–69] and numerical simulations [58, 70]. Change in the flow direction is accompanied by larger pressure losses if occurring from or to a direction aligned with the magnetic field ($\parallel B$) compared with a bend laying on a plane perpendicular to it ($\perp B$). For the latter case, the additional pressure loss due to 3D effects is expected, in fact, to be negligible compared with fully developed flow [69].

In this study, the experimental relation obtained by Reimann et al. [62] for a 90° square sharp bend parallel to the magnetic field is used to calculate k_{3D} for this geometrical element in square and rectangular ducts.

$$k_{\parallel} = 1.063\frac{c}{4/3+c} \tag{15}$$

Since inertial effects are neglected, a 180° bend can be represented by two successive 90° bends and, similarly, for intermediate value opportunely reduced coefficients are employed, i.e. $k_{60^\circ} = 0.67k_{90^\circ}$. Bends perpendicular to the magnetic field are treated using a conservative assumption such that $k_{\perp} = k_{\parallel}/3$. For circular cross-section, the same criteria are applied assuming $k_{\parallel} = 0.125$, a value proposed by Kirillov et al. [46] for insulated bends, which is then conservative for electro-conductive ones.

Cross-section variation. This class of problems has been studied analytically since the 60s [71–73] and, more recently, by experimental campaigns [38] and numerical simulations[58, 74–76]. If the rate of change is small enough, the flow can be treated locally as in fully developed state, therefore the pressure losses in a channel of axial length x_0 are described by the relation

$$\Delta p \approx \Delta p_{2D} = \int_{x_0} \nabla p(l)\, dl \tag{16}$$

where $\nabla p(l)$ is the pressure gradient for the fully developed flow described in Section 5.3.1, here assumed to be a function of the channel axial length through k_p and u_0 [46]. Conversely, sudden cross-section variations, either contraction or expansion, introduce severe 3D losses which are, in general, proportional to the change ratio. Alignment with magnetic field is found to greatly increase the irreversible pressure drop, similarly to what observed for bends. In this study, the 3D pressure coefficient is taken at $k = 0.5$ for both expansion and contraction for any change ratio. This assumption is believed to be conservative since Bühler and Horanyi reported $k = 0.315$ for an inertia-less, inviscid, sudden expansion in the magnetic field direction for a rectangular duct with change ratio equal to 4 and weakly electro-conductive duct walls ($c = 0.028$) [38].

Flow around obstacles. In this study, cylindrical obstacles transverse to the main flow direction are the most common obstacles encountered by the liquid metal. This class of problems can be considered a particular case of a gradual cross-section variation where the flow is not in local fully developed condition. Significant 3D losses are introduced if the magnetic field is transverse or aligned with the obstacle axis (*spanwise*) and, in particular, are larger for the former case [77]. Experimental and numerical studies on the subject can be found in Refs. [78–81] for transverse field and in Refs. [7, 8, 77, 82–84] for the latter situation.

The magnitude order of 3D pressure loss caused by a circular straight cylinder with blockage ratio $\beta = d/2b = 0.2 \div 0.3$ and spanwise magnetic field is estimated with the correlation proposed by Tassone et al.

$$\Delta p_{3D} = \frac{1}{2} k_o \sigma u_0 B^m d \tag{17}$$

where $k_o = 0.1931$ and $m = 1.73$ [10]. The same relation is also applied for the case of transverse magnetic field.

Flow around obstacles with more complex geometry, like U-pipes or C-pipes is scarcely reported in literature compared with the more simple straight layout. To the best of our knowledge, the only studies available are about perfectly conducting nested U-pipes, transverse to a poloidal flow, described in Refs. [9, 10]. The additional pressure drop introduced by the cooling pipes was estimated around $\Delta p_{3D} = 376.2$ Pa obstacle^{-1} for $Ha \to \infty$. This figure is adopted in the following to evaluate the pressure drop for this configuration.

Finally, the case of obstacles aligned with the streamwise direction is relevant to water-cooled blanket design adopting vertical cooling pipes [85] or horizontal ones with mostly radial PbLi flow [4]. Some works have been recently published about insulating [86] and electro-conductive pipes

[87] but, unfortunately, no information was available regarding 3D pressure losses. In this study, the pipes are assumed to do not introduce a significant effect on head loss, except for the reduction of available cross-section for 2D MHD flow. An equivalent duct of same aspect ratio and cross-section than the blanket channel is used for the pressure loss evaluation.

Non-uniform magnetic field. Magnetic field gradients can introduce additional losses with mechanisms similar to sudden cross-section variations [46]. For weak magnetic field gradients, like those present within the blanket module, the local fully developed state is assumed if the following condition is satisfied

$$\partial_x \tilde{B} = \frac{\Delta B}{B_0}\frac{a}{x_0} \ll 1 \tag{18}$$

where $\partial_x \tilde{B}$ is the normalized magnetic field gradient and B_0, a, ΔB and x_0 are reference magnetic field, characteristic length, field difference and axial length in the region where the variation occurs. Consequently, the spatially varying magnetic field within the blanket segment is assumed to do not introduce three-dimensional losses. This methodology was reported to recreate experimental data with a confidence about $\pm 10\%$ for $5 \leq x_0/a \leq 15$ [46] and it is supported by recent mock-up experiment results [88].

This treatment is no longer possible within the TFC thickness where $\partial_x \tilde{B} = 0.2 \div 0.3$. In general, three-dimensional pressure drop in a channel with non-uniform magnetic field can be calculated with the relation by Hua et al.

$$\Delta p_{3D} = k c^{0.5} p_0 \tag{19}$$

where $p_0 = \sigma u_0 B_0^2 x_0$ is the pressure scale and it is added to baseline 2D pressure loss calculated with Equation (16). For $c < 0.1$ and $2 \leq x_0/a \leq 5$ in a square duct, it is found that $k \approx 0.1 \div 0.16$ [46, 49]. A more conservative approach consists in calculating the pressure drop in the fringing field region using Equation (13) and to assume maximum magnetic field intensity. Both techniques are adopted in this study.

6. Feeding and draining pipe: results and discussion

The connection pipes with the ex-magnet section of PbLi loop are probably the most immature part of the breeder hydraulic path since very few dedicated design activities have been performed to date on these components. In this section, the influence of geometrical parameters and design choices on MHD pressure losses for these elements is going to be discussed.

6.1. Nodalization

It has previously been described in Section 4.2 that the connection pipe layout is chosen among three possible options: bottom (only for FP), mid-level, and top. Nodalization parameters are collected in Table 6. Combination of FP and DP layouts produces five integration schemes discussed in Section 4.2.

Table 6: Connection pipe nodalization [10], flow sections are shown in Figure 10

Section	Axial length (m)	Magnetic field (T)	Type
		Bottom	
FP1	1.5	1.4	2D flow
FP2	1	4.28	Non-uniform field
FP3	6.2	4.52	2D flow
		Mid-level	
DPA1	1	5.46	2D flow
DPA2	1	5.46	Non-uniform field
DPA3	0.3	0.314	2D flow
DPA4	0.46	0.909	60° Bend (∥)
DPA5	5.34	0.909	2D flow
DPA6	0.63	0.909	30° Bend (∥)
DPA7	2.3	0.483	2D flow
		Top	
DPB1	0.55	3.716	2D flow
DPB2	0.52	3.513	45° Bend (⊥)
DPB3	1.07	3.513	2D flow
DPB4	1.20	3.513	Non-uniform field
DPB5	3.95	0.284	2D flow
DPB6	0.63	0.909	90° Bend (∥)
DPB7	2.30	0.483	2D flow

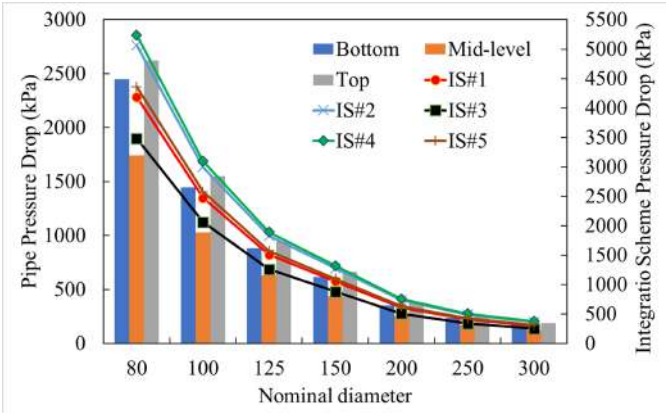

Figure 12: Pressure loss in connection pipe for three layouts (Bottom/Mid-level/Top) as function of nominal diameter, overall pressure loss for integration schemes is shown assuming same diameter for feeding and draining pipe

6.2. Baseline pressure loss

A detailed discussion of the calculation performed is available in Ref. [10], whereas results are presented in Figure 12. "Bottom" is the simplest pipe layout and does not involve any significant assumption beside for section FP1, where the poloidal magnetic field is assumed to be constant at its maximum value in the region. Real field topology is considerably more complex and involves both intensity and orientation variation along the section. In addition, inertial effects are likely to be present, affecting the flow by causing instabilities and even transition to Q2D turbulence. However, the actual pressure loss in this

section is unlikely to be higher than the current estimate due to the very conservative assumption used.

Despite extending for only 30% of the pipe axial length, section FP2 and FP3 account respectively for 30% and 50% of the overall pressure loss. In section FP2, the non-uniform toroidal field introduces a 3D effect, which is neglected by assuming only 2D pressure losses at maximum magnetic field. Adopting the relation by Hua et al. [49], a less conservative estimate is made for this flow type, which is equal to ≈60% of the previous one, by using a tanh function to approximate the fringing field[1]. Correspondingly, overall pressure loss on the pipe is equal to ≈82.5% of the conservative one that, nevertheless, it is assumed as reference in our analysis.

The same trend is found for the "Mid-level" and "Top" pipe layout where pressure losses within external TFC surface are estimated at, respectively, ≈96.8% and ≈91% of the total for ≈32.7% and ≈20% of the pipe axial length. These results can be explained with the decreased poloidal magnetic field intensity for these layouts compared with the one present in the lower port area. 3D pressure losses (non-uniform magnetic field and bends) contribute to a larger degree than for the "Bottom" layout reaching up to ≈50% and ≈47%. In the "Mid-level" pipe, nearly 33% of these losses are due to the bend within TFC, whereas in the "Top" one no relevant contribution is present except for the fringing field.

In general, the "Mid-level" layout is the one characterized by the less severe absolute losses due to the relatively low toroidal field intensity at the attachment point, which is the farthest one from the central solenoid. The same but opposite argument can be made for the "Top" layout that, although featuring only 80% of the axial length within the TFC of the "Bottom" one, has slightly higher pressure drop.

To minimize the connection pipe pressure loss is necessary to shorten and simplify the PbLi flow path within the TFC. Even if an attachment point as close as possible to the equatorial plane (i.e. lowest toroidal field intensity) could be seen as beneficial, it is really challenging to devise an efficient integration with PbLi flow path within the blanket for this option, as it will be discussed in Section 6.4.

6.3. Influence of nominal pipe diameter

It is straightforward to argue that larger pipes will be likely to feature a smaller overall pressure loss compared with tinier conduits and this is confirmed by the trend presented in Figure 12. However, it is worth noting that the linear dependence from mean velocity in Equations (13) and (14) entails a slower reduction of head loss with cross-section enlargement compared with what would be expected from a purely ordinary hydrodynamic perspective. Dependence from mean velocity is not perfectly linear either, which is caused by the discretized wall thickness values available to fit the result of Equation (10), even if the k_p perturbation introduced by varying c is quite limited (i.e. ±8% compared with DN150) [10].

[1]Exponential or sinusoidal functions can be used instead yielding a relative error ±5%

Table 7: Connection pipe (Δp_{CP}), blanket integration (Δp_{BY}) and total pressure loss (expressed in MPa) for several integration schemes taking into account pipe size limitation in the lower port

IS	#1			#2			#3	#4	#5
DN_{FP}	80	125	200	80	125	200			
Δp_{FP}	2.445	0.882	0.354	2.446	0.882	0.354	0.253	0.379	0.253
Δp_{DP}	0.253	0.253	0.253	0.379	0.379	0.379	0.253	0.379	0.379
Δp_{CP}	2.698	1.135	0.607	2.825	1.262	0.733	0.505	0.759	0.632
Δp_{BY}							0.576	0.568	0.390
Δp_{Tot}	2.698	1.135	0.607	2.825	1.262	0.733	1.081	1.327	1.022

It is not possible to choose an arbitrary pipe diameter since the connection elements must comply with size limitation, remote handling requirements, and maximum allowable pressure drop. Current state-of-the-art for remotely controlled cutting and welding tools specify an upper limit and, therefore, forbid the use of DN > 200 pipes. On the other hand, a single connection pipe should not feature a pressure loss above 1 MPa and, ideally, be lower in order to do not exceed the pressure drop limit for the whole in-magnet circuit, thus ruling out the smallest pipes.

From these basic considerations, the only feasible connection pipes in Figure 12 are 125 mm, 150 mm and 200 mm. A DN200 pipe is a good choice also for the inherent less uncertain estimate on pressure loss from Equation (13) due to large interaction parameter compared with low diameter pipes (i.e. DN 80 to 125), where inertial effects could conceivably extend for the whole pipe length.

6.4. Influence of integration scheme

In Figure 12, the four integration schemes defined in Section 4.2 are compared assuming equal nominal diameter for feeding and draining pipes. It is straightforward to observe that, as it has been discussed in Section 6.2, IS3 is featuring the lowest pressure loss due to the advantage of the "Mid-level" pipe routing compared with other options. The alternative ISs feature respectively 20%, 45%, 50%, and 25% higher head loss.

The choice of the integration scheme is constrained by size available in VV ports and internal blanket configuration. Despite being the one scheme characterized by highest loss, IS4 is the only one well suited to be integrated with configuration T03, where both distribution and collection manifold are located at the blanket top. Similarly, IS2 is the most rationale choice, despite the second worst loss, for all the other blanket configuration that, in fact, feature a mostly bottom-up internal PbLi flow path.

Feeding pipe routing through the VV lower port is constrained by the space available in the area, which is mostly devoted to maintenance and servicing of the divertor and other ancillary systems. The current integration

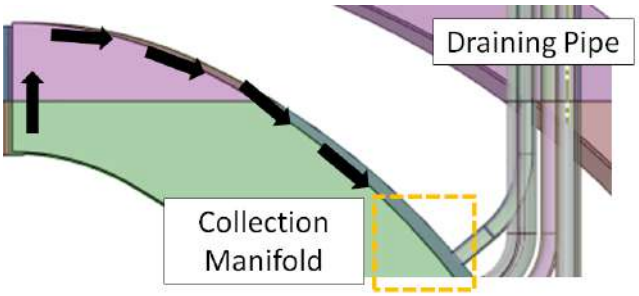

Figure 13: Integration example for IS3 and PbLi evacuation from T01.A

Table 8: Bypass channel parameters for IS3/T01.A integration

Parameter	Symbol	Value	Unit
Toroidal length	$2a$	240	mm
Radial length	$2b$	50	mm
Poloidal length (top/bottom)	L	5.18/13.11	m
Bend length	z_b	240	mm
Mean velocity	u_0	3.6	$\mathrm{cm\,s^{-1}}$
$r-p$ SP	c_1	0.1	
$t-p$ SP	c_2	0.187	
Average field (top/bottom)	$\bar{B}_t$	4.4/3.85	T

setup allows only for a DN80 pipe dedicated to provide PbLi loading and unloading, both in normal and accidental conditions, for the blanket. When this limitation is taken into account the pressure drop picture changes considerably and, as it is possible to observe in Table 7, IS1 and IS2 clearly become unfeasible. Only for a DN125 pipe the pressure drop becomes acceptable, even if nearly double the value calculated for IS not relying on the lower port routing where, however, the additional cost of integrating the connection pipe attachment and the blanket internal circuit is neglected. On this point, the opportunity cost of re-routing the feeding pipe through the upper port, which is discussed in Section 6.5, should be carefully assessed and will likely involve significant changes in the blanket internal layout.

Moreover, FP routing from the upper port introduces safety concerns about blanket drainage in accidental conditions. This function could be fulfilled by an additional drainage pipe which must be kept above PbLi solidification point. However, this solution will introduce tritium control concerns by placing stagnant PbLi close to the plasma chamber.

6.5. Blanket integration for upper port routing

Let us consider the case in which feeding and draining are executed through the upper port using the "Mid-level" routing scheme (i.e. IS3) for configuration T01.A. It is assumed that the internal PbLi flow path is unchanged, therefore the spinal manifold requires PbLi supply/evacuation from blanket extremities. Integration can be accomplished with bypass channels whose layout, sketched in Figure 13 for DP, mirrors the manifold one. Fundamental bypass parameters are collected in Table 8.

Table 9: Pressure loss (expressed in kPa) for naked and insulated pipes with progressively smaller FCI axial length L

	Nominal diameter				
Δp	80	100	125	150	200
Naked	2445.76	1445.67	882.47	616.36	353.84
$L=\infty$	652.72	299.38	157.47	88.40	39.93
$L=1$ m	713.39	349.05	198.67	122.90	66.71
$L=0.5$ m	774.07	398.71	293.88	157.41	93.49

Two successive 90° sharp ($\perp$) bends are used to connect the terminal (or initial) part of the manifold and bypass channel. Pressure loss in this components is quite limited at $\Delta p = 15.29$ kPa, whereas severe loss is encountered within the proper bypass channel due to high velocity and long axial length: 0.186 MPa and 0.360 MPa for, respectively, connection with DP and FP [10]. Integration pressure cost is equal to 0.576 MPa that, when properly accounted, makes IS3 with DN200 pipes just slightly less pressure loss intensive than the DN125 bottom feeding schemes considered in Table 7. A similar conclusion can be reached for IS5, although this scheme is affected to a lesser degree by the shorter bypass allowed by top draining, whereas overall pressure loss for IS4 is penalized for opposite reasons.

It should be noted that these considerations are somehow "optimistic" since it appears likely that to realize the bypass this one will have to be integrated within the BSS which, being more thicker and conductive than regular blanket SPs, could lead to an increased pressure loss figure than the one that has been discussed in this section. Alternative solutions could be devised by rearranging the blanket internal structure to provide less pressure loss intensive solutions, but will probably require significant design effort.

6.6. Bottom FP insulation

A possible way to retain blanket feeding from the module bottom is to curtail MHD pressure losses by forcing the fluid currents to close through the highly resistant boundary layers instead of the pipe wall. Wall/fluid electrical decoupling could allow to adopt small size pipes, thus coping with interface requirements without exceeding the allowed pressure drop as it would be the case for non-insulated (e.g "naked") conduits.

Thin insulating coatings or loosely fitted flow channel inserts (FCI) have both been proposed in past years for this purpose with the latter approach currently favored within European fusion programme[2] [89, 90]. A typical FCI is composed by a thin layer of alumina ($t = 0.1$ mm) included between two protective sheets of Eurofer ($t = 0.5$ mm) that, welded together, are then fitted inside a rectangular or circular pipe, leaving a small gap (≈ 1 mm) where the liquid metal is allowed to flow.

Recent numerical and experimental activities have shown that, despite not being able to achieve perfect insulation,

[2] R&D activities on coatings are still performed for anti-corrosion and anti-permeation barriers, see Ref. [3]

this solution can significantly decrease head loss reaching even just 5% of the naked pipe value [27, 56, 91]. Despite these promising results many open issues still remain with, among others, alumina qualification under irradiation, gap corrosion rates, and manufacturing limitations. In particular, maximum length for a continuous FCI is currently limited to about 0.5 m and insulation discontinuities are likely to be present in the blanket leading to additional losses from 3D effects. Bühler et al. observed experimentally that, for an insert one order of magnitude less conductive than pipe wall ($c_w = 0.07$–$c_{FCI} = 0.005$) and a discontinuity length $2l = 20$ mm, this additional pressure loss can be estimated with $\Delta p_{3D}/p_0 = 0.12$, where $p_0 = \sigma u_0 B_0^2 r_i$ [56].

Pressure loss in naked, continuously, and discontinuously insulated pipes with DN80–200 are presented in Table 9. State-of-the-art (0.5 m) and moderately extrapolated (1 m) FCI lengths have been used to highlight the effect of insulation discontinuity. Total equivalent FCI thickness is assumed at $t_{\mathrm{FCI}} = 15$ mm, bundling together insert and gap thickness, and used to calculate effective pipe cross-section. Gap effect on pressure loss is neglected and Eurofer sheets are considered as a single conductive strip to calculate c_{FCI}. Influence of insulation gaps on head loss is assumed uniform for all cases and taken from Ref. [56], but it is likely to be in reality a function of flow geometry and parameters, e.g. Ha, N, c_w/c_{FCI}, etc.

Even the most coarse electrical insulation considered seems able to efficiently reduce the pressure loss, since the partially decoupled DN80 pipe features about the same losses as the naked DN125 pipe. Continuous insulation pushes the loss curtail even further by making the loss in a DN80 pipe comparable to a naked DN150. If confirmed by experimental data, this mitigation strategy could potentially allow to adopt bottom FP-based integration schemes (i.e. IS1/IS2) while coping with the size limitations imposed by lower port interface requirements. Even if not strictly required, FCIs could be an attractive option for large pipes (DN > 125) where their use will be beneficial to optimize the blanket performances.

Interestingly, it can be observed how continuous electrical decoupling seems to be more efficient for large pipes ($\approx -90\%$ DN200) compared with smaller ones ($\approx -75\%$ DN80). The reverse appears to be true for discontinuous insulation, in which DN200 pressure loss more than doubles from $L = \infty$ to $L = 0.5$ m compared with a relatively modest increase for DN80 pipe. This last phenomenon is probably due to the constant value employed to assess the discontinuity loss for all pipes that, therefore, tends to penalize more a tube with a lower baseline 2D pressure loss. Even if Δp_{3D} was observed to be mostly independent by Re and Ha in Ref. [56], more experimental data is required to judge if our assumption is realistic.

Another mitigation strategy that could be used to minimize the pumping cost associated with small pipes is to branch the conduit in two (or more) elements in order to partition the PbLi flow rate and reduce mean flow velocity.

Table 10: Main geometrical parameters of compact manifold layout adopted for configuration T01.B [10]

	Symbol	Value	Unit
Toroidal length	$2a$	240	mm
Radial length	$2b$	110	mm
Poloidal length	L_{pol}	135	mm
BZ inlet diameter	D_{bz}	100	mm
SP orifice diameter	D_{sp}	78	mm
Radial-Poloidal SP	$2t_{r,p}$	16	mm
Toroidal-Poloidal SP	$2t_{t,p}$	30	mm

Table 11: Pressure losses in distribution manifold for configuration T01.B fed by two symmetrically placed DN150 FPs attached at lateral channels

Section	Flow type		Δp_i (kPa)	
	Lateral	Central	Lateral	Central
1	XS variation			18.779
2		90° Bend (‖)		1.611
3		XS variation		7.439
4		2D flow		1.538
5		XS variation		1.383
6		XS variation		7.439
7		90° Bend (‖)		0.887
8	XS variation			23.166
$\Sigma\Delta p_i$			41.945	62.192

If the conduit separation is executed far from TFC, the overall pressure loss in FP can be nearly halved thanks to linear dependence from mean fluid velocity. This solution could be desirable also for a more efficient flow distribution, as it is discussed in Section 7, since it allows to partially compensate pressure imbalances due to non-uniform blanket toroidal width. However, it is clear that this solution could be counter-productive to limit the encumbrance in the lower port. Accounting for this occurrence, it seems more useful to perform the branching as close as possible to TFC external surface, thus accepting maximum loss in the region with lowest magnetic field but minimizing port obstruction and flow velocity within the range of toroidal field.

7. Manifold: results and discussion

The manifold is the hydraulic region to which is demanded the PbLi distribution to the area tasked with the bulk of tritium breeding. As such, it is characterized by relatively small volume, high velocity, and significant geometrical complexity. In this section, the manifold layout influence on the MHD pressure loss is discussed. Four manifold layout are proposed.

7.1. Compact manifold

The "compact" manifold layout used to distribute PbLi in configuration T01.B BZ is shown in Figure 6. The component is divided into four sub-elements of equal toroidal width, labeled "lateral" or "central" channel depending on position with regard to the blanket symmetry axis, each

one directly feeding a BZ duct through a orifice drilled into toroidal-poloidal SP, called BZ inlet. Lateral and central channels are hydraulically connected through a second orifice realized on poloidal-radial SP. The flow paths marked by the yellow arrows, which distinguish between a "lateral" and "central" route, refer to the distribution manifold that, to allow the liquid metal winding into BZ, must be placed at the blanket bottom.

It is assumed that equal flow rate is distributed such that no flow imbalance is observed between the BZ equatorial plane channels. Since the blanket toroidal width is not constant, this assumptions requires the "lateral" BZ duct to gradually enlarge itself, accommodating this variation, until it branches into two separate ones, labeled "external" and "lateral" at ≈1/4 poloidal height [23, 24]. Conversely, the central duct width is approximately constant over all blanket poloidal extension. Due to this design choice and to satisfy our assumption, about 59% and 41% flow rate must be carried by respectively lateral and central channels. Neglecting electromagnetic coupling effects, this scenario will cause the formation of a significant pressure imbalance in favor of the central channel with consequent underfeeding for the others. To partially compensate for this occurrence and to take advantage of PbLi inertia, the manifold is considered to be fed by two symmetrically located DN150 FPs attached to the lateral channels.

PbLi is evacuated from the blanket through a top placed additional collector, whose geometrical parameters are identical to those listed in Table 10 for the bottom one. Due to its location, toroidal and poloidal fields for distribution manifold are taken as 4.76 and 1.4 T, whereas they are taken as 5.46 and 0.909 T for the upper collector.

Pressure loss in distribution manifold flow paths are reported in Table 11, whereas detailed calculation procedure can be found in Ref. [10]. The central sub-element features an additional ≈50% loss to carry the liquid metal from FP to BZ, mostly caused by two 90° bend plus sudden cross-section variation hydraulic elements happening parallel to toroidal field direction. Sudden expansion and contraction through SP orifice happens perpendicularly to toroidal field and it is not very expensive pressure loss-wise, accounting just for 4.5% of the total.

Main contributions to the overall loss are made by the FP/sub-channel expansion and flow through BZ orifice, both cross-section variation parallel to toroidal magnetic field, which are in common between flow paths. It is straightforward to suggest that varying BZ orifice diameter across the two flow paths can be used to regulate mass flow rate between lateral and central channels by, for instance, reducing size for the latter one. FP/sub-channel expansion is mostly related to the former component size and reaches its maximum for the smallest considered pipe (i.e. DN80) at ≈33.4 kPa. However, loss increase in this hydraulic element is negligible compared with the much more significant rise in the pressure loss of the connection pipe at the decreasing of nominal diameter, as it was discussed in Section 6.3.

If the liquid metal is supplied to the manifold with a single FP, for example with a DN200 attached to the central channel midpoint, similar to the layout shown in Figure 5 for the collection manifold of configuration T01.A, it is possible to express the pressure loss in the two flow paths by swapping them thanks to the inertia-less assumption and neglecting loss due to the very small toroidal flow length introduced. A similar layout is adopted for the collection manifold where $\Delta p = 92.443$ kPa for the lateral channel and $\Delta p = 68.28$ kPa for the central one. Manifold loss increase is entirely due to larger toroidal field in the top region and could be reduced by moving it toward the equatorial plane. However, any gain is quickly negated due to the necessary integration between the BZ flow path and draining pipe, as it was discussed in Section 6.5.

Table 12: Pressure losses in distribution collector for spinal manifold layout fed by two symmetrically placed DN150 FPs

Section	Flow type		Δp_i (kPa)	
	Lateral	Central	Lateral	Central
1	XS variation		18.779	
2	90° Bend (⊥)	90° Bend (∥)	0.564	2.255
3	XS variation	XS variation	9.378	10.415
4		2D flow		4.160
5		XS variation		1.695
6		XS variation		10.415
7		90° Bend (∥)		1.411
$\Sigma\Delta p_i$			28.720	49.130

Considering the average across manifold flow paths, overall pressure loss in T01.B "compact" collectors is estimated at $\Delta p = 132.4$ kPa, whereas for lateral and central flow paths $\Delta p_{\mathrm{L}} = 134.5$ kPa and $\Delta p_{\mathrm{C}} = 130.5$ kPa. These figures assume an integration scheme with two DN150 FPs bottom and a single DN200 DP top layout.

7.2. Spinal manifold

The "spinal" layout used to distribute PbLi in configuration T01.A, which is presented in Figure 5, is divided into three components: two terminal collectors, placed at the blanket extremities and called distribution/collection manifold, and a spinal collector, connecting the other two elements. The latter manifold is the most important one and is composed by two parallel rectangular arrays of poloidal channels: the internal one, called supply leg (SL) and that distributes liquid metal to the BZ cells, and the external one, called recovery leg (RL) which collects PbLi exiting the blanket. Indeed, the terminal collectors allow PbLi to distribute across spinal manifold channels and are correspondent to their terminal part, from which the name.

7.2.1. Terminal collectors

Geometrical parameters for the terminal collectors are close to the one listed for compact layout in Table 10, the only difference being radial length $2b = 40$ mm and SP orifice diameter $D_{sp} = 70$ mm. The flow map is very similar to the one discussed in Section 7.1 with "lateral" and "central" sub-elements distributed across the blanket

Table 13: Toroidal width, in mm, of poloidal channel versus spine linear length (S) and vertical coordinate (Z)

			Toroidal width		
Z (m)	S (m)	No. channels	External	Lateral	Central
-6.88	0	4		240	240
-3.70	4	4		336	234
-3.60	4.1	6	86	234	234
0.583	8.55	6	217	234	234
3.59	11.75	6	86	234	234
3.60	11.76	4		336	234
6.76	16.93	4		240	240

symmetry axis, connected by an orifice drilled on the radial-poloidal SP. The liquid metal flows toroidally through the channels and then turns in the poloidal direction, flowing in the main manifold channels. Following this similarity, the manifold is fed by two DN150 FPs placed at the center of lateral channels to minimize the pressure differential across flow paths. Again, distribution and collection manifold are located at the lowest and highest position in the blanket, therefore the magnetic field intensities are equal to those employed for the compact manifold estimation in Section 7.1.

Pressure loss in distribution manifold flow paths are reported in Table 11, whereas detailed calculation procedure can be found in Ref. [10]. Central flow path features an additional ≈70% loss compared with lateral one, again due to the two 90° bends and XS variation parallel to the toroidal field. Biggest loss contribution is caused by FP/sub-channel expansion, as it was for the compact manifold. Same general behavior is shared between configurations for feeding through a single FP. In the collection manifold, the pressure loss is slightly higher due to different toroidal field, amounting to $\Delta p_{\mathrm{L}} = 64.926$ kPa for the lateral path and $\Delta p_{\mathrm{C}} = 24.370$ kPa in the central one. These values are reduced to $\Delta p_{\mathrm{L}} = 30.879$ kPa and $\Delta p_{\mathrm{C}} = 10.833$ kPa for a position consistent with mid-point DP attachment but, as it was for the compact layout, the loss reduction for the change in manifold location is quickly offset by enhanced loss within integration elements.

7.2.2. Poloidal channels

A spinal manifold channel is characterized by a radial-toroidal cross-section $2b \times 2a$, where $2b = 30$ mm. Conversely, the toroidal width ($2a$) is a variable being function both of poloidal position and flow path type due to the widening from blanket extremities to equatorial plane. In Table 13, the toroidal width is presented for three manifold flow paths taking into account the blanket linear length S =0÷16.93. The "lateral" channel gradually enlarges until it branches in two and, at the equatorial plane, all the channels have approximately the same width. The reverse trend happens moving toward the blanket top, where the external and lateral channels gradually shrink; the central channel by comparison is almost unchanged throughout the entire length. In addition, flow rate is progressively

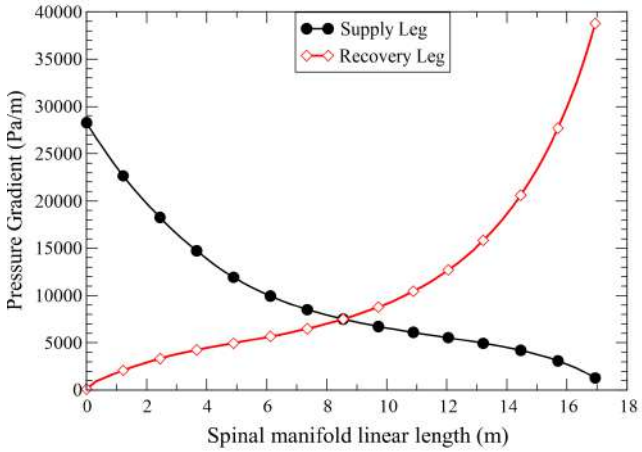

Figure 14: Pressure gradient for central channel supply and recovery Leg

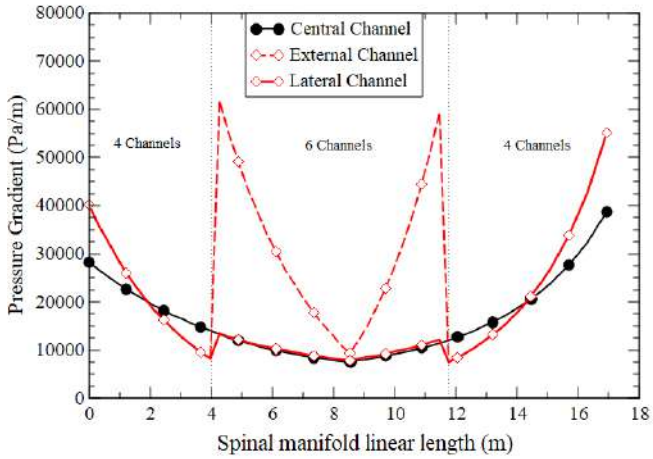

Figure 15: Pressure gradient for central, lateral, and external channel following the maximum pressure loss flow path, i.e. BZ cell located at $S = 8.55$ m

decreasing along a SL channel while the liquid metal is distributed across BZ cells, whereas the opposite happens along the RL channel. It is straightforward to deduce that pressure loss in the manifold channel will depend both by the poloidal and toroidal position of the BZ cell fed.

Let us consider first a BZ cell fed by a "central" channel, where it is possible to neglect the toroidal width enlargement. The mean channel velocity is assumed to decrease continuously and that it is possible to approximate its variation with a linear function without any loss of generality compared with a more realistic step function, where a discretized flow rate $\Gamma/6N_{\mathrm{cell}}$ is deviated toward a BZ cell every $S_{\max}/N_{\mathrm{cell}} \approx 0.135$ m. The pressure gradient in the SL and RL channel will have the trend shown in Figure 14: the maximum gradient in the RL is slightly higher than for SL due to the stronger toroidal field experienced at maximum flow rate carried, i.e. top versus bottom. For an arbitrary cell at S_i, the total pressure loss will be given

by the sum of the SL plot integral in the range S=$S_{\min}$–S_i and RL plot integral in $S = S_i$–$S_{\max}$. The maximum pressure loss is observed for a cell located slightly above the equatorial plane at $S = 8.55$ m, for which $\Delta p_C = 269.74$ kPa, whereas the minimum loss is found for the topmost cell ($S = 16.93$ m), for which $\Delta p_C = 168.21$ kPa.

Considering now the lateral and external flow path, the effect of gradual cross-section (and aspect ratio) change on the pressure gradient must be taken into account. It is assumed that the lateral channel branching does not introduce any significant 3D effects or, in other words, that the flow does not depart from the local fully developed state necessary to apply Equation (16). Moreover, the assumption that flow rate must be equally distributed across the BZ cells is maintained. In Figure 15, the attention is focused on the most loss intensive BZ cell, i.e. located at $S = 8.55$ m, for all the flow paths. In the lateral channel, the pressure gradient is initially higher than for the central channel due to larger mean velocity but drops quickly due to the combined effect of increasing available cross-section and aspect ratio, since $k_p \propto (a/b)^{-1}$, and it becomes lower than the central channel at $S \approx 2$ m. After the branching, it is the external channel to widen, whereas the lateral toroidal width remains constant and, consequently, its pressure gradient becomes comparable to the one in the central flow path. Due to its initial small width, the external flow path is penalized by as much as five times the pressure gradient in the other channels. This occurrence reflects on the total loss where, for the cell at $S = 8.55$ m, $\Delta p_E \approx 442$ kPa and $\Delta p_L \approx 285$ kPa.

Neglecting electromagnetic coupling effects, the large pressure difference (≈ 150 kPa) between external and lateral flow path strongly suggests an overfeeding of the latter, which will results to pressure equalization about at $\Delta p_L \approx 340$ kPa. However, this situation will lead to a pressure difference (≈ 70 kPa) in favor of the central channel, thus likely leading to further flow rate redistribution and severe underfeeding of the smaller external channels. This scenario is not particularly concerning for the blanket thermal-hydraulics, due to the low PbLi velocity envisioned, but rather for the tritium inventory control, since it could potentially introduce a large volume of almost stagnant breeder in the component.

7.2.3. Influence of internal obstacles

In Figure 5, it is shown that the connection between BZ and manifold RL is ensured by a large pipe crossing the SL duct. Coolant pipes are also required to go through the manifold channels, further blocking part of the available cross-section and likely introducing additional losses. Let's focus our attention on the BZ outlet pipe to estimate the obstacle contribution to the SL losses for two reasons: it is the largest element ($\beta = d/2a \approx 0.2$ for $d = 50$ mm int the central channel) and is equal for all the flow paths. Conversely, cooling pipes in the C-layout have smaller contribution to the blockage ration and mostly affect the lateral channels, even if they extend in both the manifold arrays.

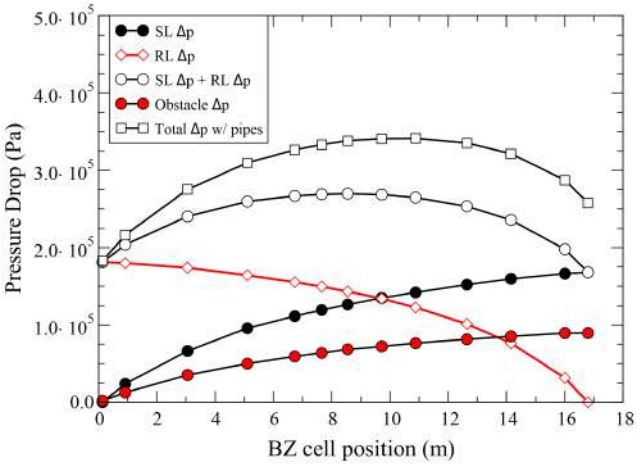

Figure 16: Obstacle effect on supply leg and overall pressure drop for an arbitrary BZ cell fed by the central flow path

Assuming $d = 50$ mm, a rough estimate of the obstacle pressure loss can be obtained through Equation (17). For the central channel mean velocity and magnetic field (i.e. $u_0 = 2.7$ cm s^{-1} and $B = 3.79$ T), the mean specific obstacle loss is evaluated at $\Delta p_{o,C} = 1.02$ kPa per pipe. In the lateral channel, where mean velocity is higher due to increased flow rate this value is slightly superior at $\Delta p_{o,L} = 1.18$ kPa per pipe.

The overall impact of the obstacles on manifold pressure drop is dependent on the BZ cell location: the total obstacle loss for an arbitrary cell located at $S = S_i$ along the blanket spine is dependent by the number of cells below the one considered, i.e. the number of pipes crossed by the PbLi in its SL path $N = S_i/H$ with H being the BZ cell poloidal height projected on the blanket spine. Obstacle loss will be higher for BZ cells located at the blanket top, whereas becomes negligible moving toward the bottom, as it is shown in Figure 16, thus possibly causing overfeeding for cells with a lower position.

Under our working assumptions, the obstacle loss affects only the SL channel and, thus, shifts to $S \approx 10.8$ m the spinal position of the most loss intensive BZ cell. However, the combined (SL+RL) loss plot is mostly flat around $S = 8 \div 12$ m, thus the difference with the cell at $S = 8.55$ m is below 2%. For this cell, the obstacle loss can be estimated as 65.444 kPa for central flow path and 75.248 kPa for the lateral one. Since only the BZ outlet pipe has been considered in this preliminary estimate, these figures are likely to increase in a more complete dissertation that will include the water pipe effect on blockage ratio, which will probably result in a larger pressure difference between lateral and central channels.

It should be noted that the PbLi flowing in the connection pipe is in electrical contact with the wall and such tube is immersed, in turn, in the upward flow happening

Table 14: Overall pressure loss of the spinal manifold (in kPa), external and lateral flow paths are assumed to be equal

	Lateral	Central	$\Delta p_i/\Delta p$ (%)
Distribution	28.720	49.130	5.56/12
Spinal			
• 2D flow (SL+RL)	340	269.74	66.8/66
• Obstacle	75.248	65.444	14.8/16
Collection	64.926	24.370	12.8/6
Total	508.894	408.684	100/100

in the manifold channel, thus they will be electromagnetically coupled through mutual leakage currents. To the best knowledge of the authors, such a cross-flow case has never been investigated in the literature and could have unforeseen consequences on the pressure drop estimate and flow features within both the BZ outlet pipe and larger manifold channel.

7.2.4. Summary for spinal manifold

An overview of pressure loss in the spinal manifold, broken down by component contribution, is presented in Table 14. Terminal collectors play a minor part in determining the overall loss, accounting for a little less than 20%, and are comparable to the influence of obstacle in the poloidal channels. A significant pressure difference is found between lateral and central flow paths which could lead, neglecting distribution phenomena triggered by electromagnetic coupling, to the overfeeding of these last ones. In particular, large differential with the more external channels is predicted, which could lead to a consistent part of the blanket volume to be almost stagnant, introducing issues for tritium breeding and control. Manifold complexity makes difficult to predict how the liquid metal will distribute across the blanket and, even if a uniform flow rate is not required within BZ cells for thermal-hydraulic purposes, ensuring an active circulation of the PbLi everywhere in the blanket is of paramount importance.

7.3. Plenum manifold

In this section, the plenum manifold layout effect on MHD pressure losses is discussed. Here, a "plenum" is a cavity devoted to PbLi distribution that is obtained by removing SPs and other internal structural elements from a blanket chunk of poloidal height H at the segment extremities. In Figure 9, two separate plena are realized at the blanket top to handle PbLi distribution for configuration T03: the upper (and larger) one is dedicated to retrieval, whereas the lower, smaller, collector directly feeds the downward channels. In Figure 8, it is shown how the same layout is adapted for configuration T02: here, a "feeding" plenum is created at the blanket bottom, whereas a identical one will be present at the top to collect the fluid. However, removal of structural elements could be unfeasible in this blanket type since it could lead to mechanical instability of the bottom cap, which is subjected to significant hydrostatic load. To address this issue, the SPs arrangement is preserved in the honeycomb layout, which will be discussed in Section 7.4.

Table 15: Plenum geometrical parameters

	Symbol	mm
Central ch. toroidal width	$L_1/L_2/L_3$	110
Lateral ch. toroidal width	L_4	120
Poloidal height	H	242
Back ch. radial width	R_1	167
Front ch. radial width	$R_2/R_3/R_4$	147
BSP orifice diameter	d	100
Radial-Poloidal SP	t_1	16
Toroidal-Poloidal SP	t_2	19
FW/BSP	t_3	25

Table 16: Minimum and maximum loss per channel in distribution plenum for configuration T02 fed by a single DN200 FP

Section	Flow type	Δp_i (kPa)	% (min/max)
1	XS variation	25.144	82.2/72.5
2	Plenum flow	1.303÷5.411	4.3/15.6
3	90° Bend ($\perp$)	0.163	0.5/0.5
4	XS variation	0.942	3.1/2.7
5	XS variation (BSP)	3.037	9.9/8.8
$\Sigma\Delta p_i$		30.590÷34.698	

7.3.1. T02 plenum

Distribution and collection plena for this configuration are identical, if inertial effects are neglected, with the only difference being the applied magnetic field intensity. This parameter is taken equal to that one adopted in Section 7.1, except for the toroidal component in the distribution plenum, where 4.87 T are considered to account for the component extension in the radial direction compared with the compact layout. No change in our assumptions is required for the collection plenum, since the blanket has almost no depth in the radial direction there.

Plenum layout is shown in Figure 8, where BZ SPs are represented by dashed lines, the cavity is separated from the BZ by a bottom support plate (BSP) placed at $H = 242$ mm from the cap. Geometrical parameters are collected in Table 15. Orifices are drilled on the BSP to allow PbLi flow to/from the BZ with $d = 100$ mm, which means that approximately 38% of the plate surface is dedicated to this function. Each BZ channel is identified by a radial (i) and toroidal (j) rank (C_{ij}) in the grid described by Figure 8, its pressure drop will composed by a fixed term (contributions from section 1 and 3÷5 in Table 16) and a variable term (section 2 in Table 16), representative of the loss due to radially and toroidally aligned 2D flows within the plenum.

Since for each radial or toroidal rank a fourth of the flow rate is redirected toward the BZ, it is straightforward to deduce that specific plenum loss is decreasing advancing through ranks, i.e. loss for the first toroidal rank is lower than for the last, and that the BZ channel C_{11}, which is the closest to the FP, will feature the lowest loss, whereas C_{44} will have the highest. However, the main contribution

Table 17: Minimum and maximum loss per channel in distribution plenum for configuration T03 fed by a single DN200 FP

Section	Flow type	Δp_i (kPa)	% (min/max)
1	XS variation	31.606	72.5/66.1
2	Plenum flow	1.591÷5.795	3.6/12.1
3	90° Bend ($\perp$)	0.411	1.0/0.9
4	XS variation	2.368	5.4/5.0
5	XS variation (BSP)	7.636	17.5/16.0
$\Sigma\Delta p_i$		43.612÷47.816	

to the manifold loss is from the fixed term with, in particular, the FP/plenum expansion accounting for 72.5÷82.2%, therefore no relevant pressure differential is introduced across the BZ channels in the manifold. Overall loss can be slightly reduced by considering a scheme with two FPs, as discussed in Ref. [10] with complete calculation methodology as well. Loss in the collection manifold is higher at $\Delta p = 38.374 \div 43.274$ kPa due to increased field intensity, but overall behavior is unchanged thanks to inertia-less assumption.

Mechanical stability of the bottom cap is a big concern for this layout due to both the large hydrostatic load and the over-pressurization transient peak that must be withstand by the structure. Detailed thermo-mechanical analyses for this configuration are not currently available and its feasibility is unclear. Due to the low manifold losses, it could be possible to reinforce the bottom segment by reducing penetration surface on BSP or thickening it without drastically increasing the overall estimate. However, it should be noted that, since the manifold extends as far as the FW, it would be subjected to relevant volumetric heating: effect of cooling system on losses and flow distribution could potentially be significant.

7.3.2. T03 plenum

Geometry of the T03 plena are shown in Figure 9. Distribution manifold is very similar to the one discussed for configuration T02 in Section 7.3.1, with the only difference being that only two radial ranks are present and, therefore, half of the flow rate is redirected in the poloidal direction, pass through the separation plate, and enters BZ channels for each rank. Terminal collector layout is, again, very similar to the previous one, but after the second radial rank, all the flow rate is carried by a single channel (labeled C_0 in Figure 9). Thanks to this magneto-hydraulic similarity, let's assume that losses in the T03 plena can be calculated with the same methodology applied in Section 7.3.1 with only minor update to geometrical parameters and flow map. Detailed calculation is presented in Ref. [10], whereas an overview of the results for distribution plenum is available in Table 17.

Fixed loss term is also dominant for this configuration, even more than for T02 plenum, due to enhanced flow velocity in the elements characterizing the fluid movement from the manifold to the BZ channel. Overall behavior is similar and it does not merit additional discussion. Large

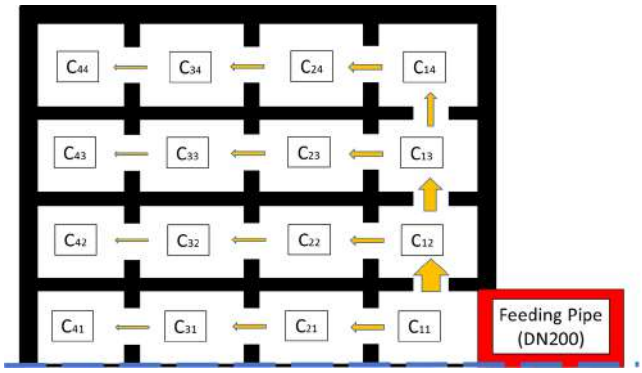

Figure 17: T02 honeycomb manifold layout and flow map, radial-toroidal view, dashed line identifies symmetry axis, arrow width is proportional to flow rate

Table 18: Minimum and maximum loss per channel in distribution honeycomb for configuration T02 fed by a single DN200 FP, percentage contribution refers to the most loss intensive channel

Section	Flow type	Δp_i (kPa)	%
1	XS (FP)	25.144	38.7
2	2D flow	1.862÷7.795	12.0
3	XS (TOrif)	0÷4.26	6.6
4	90° Bend $r \rightarrow t$ ($\parallel$)	0÷5.892	9.0
5	XS (ROrif)	0÷20.087	30.9
6	90° Bend $t \rightarrow r$ ($\parallel$)	0÷0.705	1.1
7	90° Bend $t \rightarrow p(\perp)$	0.164	0.3
8	XS variation	0.941	1.4
$\Sigma\Delta p_i$		28.113÷64.988	

terminal channel (C_0) in the collection plenum makes the loss in this component approximately equal to the distribution collector, being in the range $\Delta p = 45.968 \div 50.842$ kPa despite the higher toroidal field.

Mechanical stability issues are less concerning for T03 plena thanks to their placement below the upper cap. Nevertheless, detailed analyses are required to assess if the structure weakening negatively influences the blanket behavior during over-pressurization transient. Similarly to the T02 plenum, collection manifold must be refrigerated due to the proximity with the FW. Impact of vertical obstacles on 3D pressure losses is difficult to predict since no similar geometry has been ever investigated in literature.

7.4. Honeycomb manifold

In the honeycomb manifold, shown in Figure 8, the SPs arrangement is preserved to do not alter the cap mechanical stability, whereas orifices are drilled on the radial-poloidal and toroidal-poloidal SPs to allow the PbLi flow across the terminal part of the BZ channels. Assuming feeding from a single DN200 FP, the flow map for this component is presented in Figure 17, where the collector seen from above resembles an honeycomb with rectangular cells. Geometrical parameters are analogous to those present in Table 15, where the BSP orifice diameter is substituted by that for radial-poloidal ($d_{r,p} = 143$ mm) and toroidal-poloidal ($d_{t,p} = 92$ mm) orifices, which account

for, respectively, 40% and 25% of the associated channel cross-section.

Akin to the plenum layout, each BZ channel is associated to a toroidal and radial rank depending on its placement which, in turn, determines the flow path (shown in Figure 17) and pressure loss. This last one will be composed by a fixed and variable term, which is related to the specific loss due to the channel position. It is straightforward to observe that a duct placed on the first toroidal rank (i.e. C_{1j}) will not have any loss due to sudden contraction and expansion through a radially oriented orifice (ROrif), whereas one located on the fourth radial rank (i.e. C_{i4}) will have three separate contributions from this hydraulic element. Similar arguments can be made for flow through toroidally oriented (TOrif) orifices and bends, which are necessary to move PbLi within the manifold. Detailed calculation methodology is described in [10], whereas a results overview is presented in Table 18 for the distribution manifold.

A large number of hydraulic elements depending on the channel position causes inevitably a rise in the variable compared with the fixed term for this manifold layout: the latter accounts for only 40% of the overall drop in the honeycomb, compared with nearly 90% observed for the plenum. Pressure differential is mainly found across channels belonging to different toroidal ranks due to the huge contribution from the flow through radially oriented orifices, whereas the contribution from larger toroidally ones is almost negligible, amounting to no more than 7% of the total. Switching to a feeding scheme using two FPs does not significantly reduce the overall loss in the manifold since it will mainly counter this last term.

Since channel loss is strongly sensitive to radially oriented orifice diameter, it could be conceivable to iterate on the manifold design in order to find the optimal diameter for each orifice to minimize pressure imbalance across channels. However, uncertainties about the estimate for small orifices, which could be dominated by the inertial regime, suggest that extensive 3D simulations will be required for this purpose. Cooling requirement for this layout do not differ from that expected for the plenum, although the more complex geometry will certainly force to devise an *ad hoc* cooling system, where the pipes are likely to be routed through the radial orifices. This solution will inevitably lead to a loss increment, but it is very difficult to predict how much this will affect the current figure, which is already nearly double that expected for the plenum layout.

7.5. Influence of manifold layout

Four manifold layout have been discussed in this section to transfer PbLi from the connection pipe (being FP or DP) to each configuration BZ, in order of geometrical complexity: plenum, compact, honeycomb, and spinal. Not all these choices are suitable for all the blanket configurations since, for instance, the spinal manifold is specifically tailored to the numerous, separated, mostly radial cells adopted in T01.A, whereas the plenum layout is best suited for a blanket where the flow is poloidally oriented like in T02 or T03. Large differences are observed across these proposed models and, therefore, it is difficult to directly compare their performances, although some general observations can be made.

Table 19: Qualitative comparison between manifold layouts according to five FoMs, WF stands for weight factor

	WF	Compact	Spinal	Plenum	Honeycomb
Flexibility	4	2	4	2	2
Cooling	5	5	4	2	1
Integration	6	3	4	1	2
Distribution	8	4	2	5	3
MHD loss	10	3	1	5	2
Σ_i(WF×score)		113	86	114	69

To fulfill its assigned function the PbLi manifold should ensure uniform flow rate distribution across BZ channels and minimize MHD pressure loss. At the same time, its layout should not significantly affect the blanket mechanical stability in normal and accidental conditions or introduce concern about tritium generation and control. Manifold layout can affect mechanical stability either by altering SP arrangement or not foreseeing sufficient PbLi cooling. Pre-conceptual R&D blanket activities have been mainly focused on BZ design, and rightly so, since this region is the most important for power extraction and fuel breeding but, consequently, SPs placement often did not take into account the necessity to reserve space for PbLi collectors; a similar argument can be made for the cooling system. Therefore, ease of integration within the blanket, "structural" and "thermal" is a figure of merit (FoM) that must be considered. Moreover, a certain degree of "flexibility" is beneficial for the manifold since interface requirements could be altered to accommodate mutated integration needs with other reactor systems, e.g. divertor or PbLi loop.

A qualitative comparison between the four manifold layouts is presented in Table 19 using five figure of merit: flexibility, ease of cooling system integration, ease of mechanical integration, efficiency of flow distribution, and MHD pressure losses. Weight factors have been introduced for each FoM with flexibility and MHD loss rated as the least and most important ones. At each manifold layout is associated a score in the range 1 to 5. A relatively simple and straightforward geometry allows to minimize pressure loss and imbalance in the plenum layout, thus resulting in good scores for the most important FoM, but will require significant investment in R&D activities to adapt it for T01.A and T01.B, where the BZ PbLi flow is mostly radial, and to assess its impact on the blanket mechanical and thermal behavior. Conversely, the spinal layout is penalized by the largest loss, even if it is very well integrated in the blanket, as far as being able to drastically modify its feeding scheme without large modifications.

Assessing flow distribution in the manifold is a challenging task since it requires to include the influence of both electromagnetic coupling and inertial phenomena, these

Table 20: T01.A BZ channel geometrical parameters

	Symbol	mm
Toroidal width	$2a$	234
Poloidal width	$2b$	60.5
Cell poloidal height	H	135
Radial length	R_1	400
Bend length	R_2	150
Double Walled Tube diameter	d	13.5
Radial-Poloidal SP	$2t_{r,p}$	19
Toroidal-Radial SP	$2t_{r,t}$	12
Baffle Plate thickness	$2t_b$	2
FW thickness	$2t_{FW}$	25

Table 21: Pressure loss for T01.A BZ equatorial cell

Section	Flow type	Δp_i (kPa)	%
1	XS var. (Inlet)	1.817	39.0
2	90° Bend ($\perp$)	0.151	3.3
3	XS var. (Duct)	0.091	2.0
4	2D flow	0.157	3.7
5	180° Bend ($\perp$)	0.044	1.1
6	Obstacle (n=13)	0.025	0.6
7	XS var. (Outlet)	0.091	1.1
8	2D flow	0.323	6.8
9	90° Bend ($\perp$)	0.151	3.3
10	XS var. (Manifold)	1.817	39.0
$\Sigma\Delta p_i$		4.667	

latter being magnified especially for compact or convoluted geometries. If the flow distribution in the plenum can be attributed almost exclusively to pressure imbalance across BZ channels, the same argument does not hold in other layouts. For instance, the large differential between lateral and central channels in the spinal manifold suggests the overfeeding of these but, on the other hand, if a double FP scheme is adopted strong inertial effects in the small terminal collectors could partially compensate for this occurrence. Coupling across SL and RL channels could also affect the fluid distribution and behavior by, for instance, promoting flow rate in central channels or counter-flowing in nearby ducts, this last case being likely at blanket extremities where $\Delta\Gamma$ is large across the two arrays [44, 45, 92]. Similarly, inertial effects could play a large role in determining flow distribution in compact and honeycomb collectors. Detailed 3D CMHD analyses are deemed essential to characterize these phenomena even if, currently, they present exorbitant computational costs.

8. Breeding zone: results and discussion

8.1. Quasi-radial flow (T01.A)

The BZ basic layout, outlined in Figure 4a and Figure 4b, is composed by an elementary cell divided into six separate channels, where the PbLi is mostly radial, with each one being fed by an associated manifold duct, as discussed in Section 7.2. This elementary cell is then repeated in the poloidal direction, thus filling all the available BZ volume. However, cell geometry is not uniformly constant due mainly to constraints exerted by the overall segment geometry, i.e. decrease of toroidal width at blanket extremities reduces the number of BZ ducts from six to four; a similar behavior is observed also for configuration T01.B in Section 8.2. Cooling system uses a C-pipe layout where twenty-one horizontal pipes enter radially the cell from the side channels and becomes toroidally oriented moving toward the center.

Consider the central duct of a cell close to the equatorial plane, where cooling pipes are transverse to flow direction, thus allowing treatment via eq. (17), and cross-section is constant. Results obtained under these assumptions will be qualitatively similar to the other channel types and will be also be representative for different location within the blanket where, under the assumption of uniform flow distribution, the only boundary condition that must be changed is the magnetic field intensity and orientation.

The flow rate (and mean velocity) in the central channel is estimated from the total number of elementary cells in the BZ. From main geometrical parameter listed in Table 20, it is found that $N \approx S_{FW}/H \approx 109$, where $S_{FW} = 14.67$ m is the BZ linear length calculated at the first wall, thus $\Gamma_i = \Gamma_{OB}/6N = 25\ \mathrm{g\,s^{-1}}$ and $u_0 \approx 0.18\ \mathrm{mm\,s^{-1}}$. Therefore, velocity in the duct is vanishingly small and it can be expected for the pressure loss to be similarly reduced.

Interface with the manifold region is provided through an inlet opening (SL/BZ) and an outlet pipe (BZ/RL), as it was shown in Figure 5. The inlet opening is basically a round orifice, with $d = 43$ mm, drilled in the toroidal-poloidal back plate separating manifold and BZ. The outlet pipe is characterized by the same internal diameter but, since it crosses the SL duct, has also an outer diameter $d_o = 50$ mm and an axial length $L = 100$ mm, which allows to estimate a 2D flow contribution.

An overview of the pressure loss estimate is given in Table 21, which is broken down into three distinct groups of hydraulic elements: path from the manifold supply channel to the BZ duct (via the inlet opening), flow within the duct, and exit to the retry channel (through the BZ outlet pipe). The very low velocity in the BZ channel causes limited pressure losses in this hydraulic region. Indeed, they could be neglected without significantly altering the pressure drop estimate for the whole configuration since they amount to ≈1% of the manifold pressure drop. This is not a surprising outcome, because this layout was purposefully designed to achieve the lowest possible pressure drop. Largest loss contribution is found for the interface elements with the manifold, whereas pressure drop in the actual BZ is almost negligible. 3D losses in the cell amount to more than 60% of the total and, in particular, cooling pipe effect is predicted to be low (≈5%).

BZ cells located toward the blanket terminal parts are exposed to a stronger magnetic field intensity but, even in their case, the maximum pressure drop is found to be $\Delta p_{BZ} \approx 11.5$ kPa, thus never exceeding 3% of the manifold loss. It can be concluded that pressure imbalance across

cells is mostly caused at manifold rather than BZ level and, therefore, for this configuration is important to carefully regulate the pressure losses in the former component to achieve an uniform flow distribution.

Electromagnetic coupling phenomena in this configuration are expected to appear at channel, cell, and blanket level. Since the single BZ channel is composed by two counter-flowing ducts, leakage currents are expected to reorganize the flow on cross-section, for instance, by promoting the jet that appears close to the thin baffle plate [5, 42, 43]. As an assembly, the cell channels are stacked in the magnetic field direction and are going to be coupled through radial-poloidal SPs, i.e. Hartmann walls. Limited effect is envisaged for this coupling type, as it was described in Refs. [44, 45], which is mostly restricted to a slight increase of the flow rate in the central channels. At blanket level, the system can be seen as six separate poloidal columns composed by alternate counter-flowing channels which are coupled through toroidal-radial SPs, i.e. walls parallel to main magnetic field. In this scenario, overfeeding of cells at blanket extremities is expected, whereas suppressed flow rate should be observed on the equatorial plane cells [44]. Obviously, it is difficult to predict how coupling phenomena are going to affect the liquid metal at this level and, even more so, how they will interact with the effects at channel and cell level.

Some insight can be deduced from Ref. [42], where a similar configuration, composed by counter-flowing block of six channels aligned in the poloidal direction, was studied numerically. If a significant poloidal field is present, the channels are strongly coupled and the solution appears to ignore dividing SPs with flow features, like core and internal layers, being "transferred" across nearby channels. It is not clear how this result can be extended to a sequence of counter-flowing single channels, like the present configuration, but it is probable that the actual flow behavior will resemble the general trend for coupled ducts stacked perpendicularly to the magnetic field, i.e. depressed and enhanced flow rate, respectively, at stack core and extremities [44]. Experimental findings on a scaled-down mock-up seems to confirm this scenario where BZ pressure loss for external units was observed to be between four and five times higher than in central ones [19]. Velocity profile reconstruction *a posteriori* confirmed the presence of enhanced flow rates [93].

These effects could combine with the imbalance predicted at manifold level to cause underfeeding of equatorial cells. However, the BZ flow velocity is already so low that no significant influence is foreseen for pressure drop and heat transfer estimate. Conversely, stagnation or reversal regions are likely to occur and could lead to tritium inventory issues and enhanced permeation rates.

8.2. Radial-poloidal flow (T01.B)

This configuration is composed by continuous channels that wind up through the blanket, starting from the bottom and proceeding to the top. Its BZ layout is very similar to the one described for T01.A and, in fact, can be obtained from this one by removing the baffle plate, thus merging the inlet and outlet duct of the previous layout, and shortening the toroidal-radial SP to leave a connection gab at FW, as shown in Figure 4c. Space allocated for the spinal manifold is "re-purposed" in T01.B to allow the PbLi to execute another 180° turn and close the channel loop. Cooling system layout is maintained without modifications. Geometrical parameters are equal to those presented in Table 20, with the exception of $2b = 123$ mm and $H = 270$ mm, adding $R_3 = 150$ mm for the back hairpin turn.

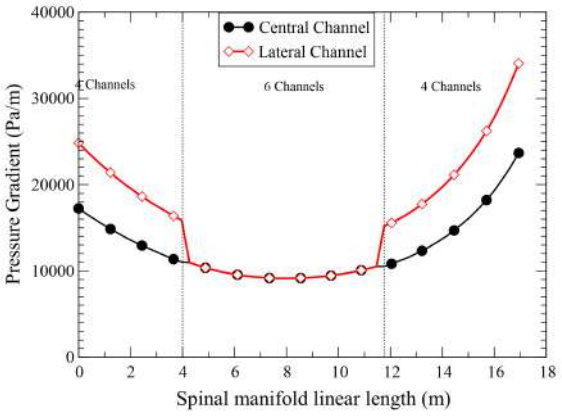

Figure 18: Baseline pressure gradient for central and lateral channel in T01.B breeding zone

Table 22: Pressure losses in T01.B BZ sub-element belonging to central flow path

Section	Flow type	Δp_i (kPa)	%
1	180° Bend (⊥)	0.549	1.9
2	2D flow	17.318	60.1
3	XS variation	7.154	24.8
4	180° Bend (⊥)	0.497	1.7
5	Obstacle	3.365	11.7
$\Sigma\Delta p_i$		28.883	

Taking into consideration the minimal channel geometry, the BZ flow path is composed by fifty-four sub-elements. Each duct carries approximately $\Gamma_i = \Gamma_{OB}/6 = 2.73\,\mathrm{kg\,s^{-1}}$, which correspond to an average velocity $u_0 = 1.16 \div 1.67$ $\mathrm{cm\,s^{-1}}$, the latter value referring to the lateral channel, nearly a hundred times the velocity envisioned for T01.A.

Since the BZ channel is extended for all the blanket poloidal length, the baseline pressure gradient for fully developed flow is far from uniform and must be discussed with the same procedure outlined in Section 7.2.2. An overview of the results is presented in Figure 18, where it is possible to see that 2D loss follows the same behavior previously described for the poloidal channels of the spinal manifold. The average pressure gradient in the breeding zone is calculated as $\nabla\bar{p}_c = 12.394\ \mathrm{kPa\,m^{-1}}$ and $\nabla\bar{p}_l = 15.951\ \mathrm{kPa\,m^{-1}}$. Defining the average sub-element length

as $L = 2 * R_1 + R_2 + R_3 + H = 1.34$ m, the total 2D loss is estimated at $\Delta p_{c,2D} = 896.5$ and $\Delta p_{l,2D} = 1154$ kPa.

Four components are responsible for 3D losses: two 180° bends ($\perp$ B), sudden contraction and expansion at BZ/turn–back interface, flow around obstacles. To evaluate the hairpin bend close to the FW the average field in that region is used ($B = 4.19$ T), whereas for the other elements the average field intensity on the whole channel radial width is adopted ($B = 3.91$ T). Number of pipes crossed by the average flow path for sub-element is twenty-six. Overall estimate is collected in Table 22 for the central channel portion on the equatorial plane.

Higher PbLi velocity increases the share of 2D losses compared with T01.A and, moreover, it is significant that the contribution given by the flow around cooling pipes reaches up to 11%, the largest 3D loss beside the cross-section variation from the main BZ duct and the turn-back region. It is possible to characterize the ratio between two-dimensional and three-dimensional losses for the single sub-element with the parameter $\psi = \Delta p_{3D}/\Delta p_{2D} = 0.67$, which describe the relative importance of the three-dimensional effects compared with baseline pressure loss. It can be then used to estimate the overall magnitude of three-dimensional losses on all channel sub-elements through the relation $\Delta p = \Delta p_{2D} + \psi \Delta p_{2D}$. Therefore, overall loss on central and lateral flow path are evaluated, respectively, at $\Delta p_c = 1545$ and $\Delta p_l = 1985$ kPa.

These pressure losses are much higher than those predicted for other blanket configurations mainly due to the long, windy, PbLi path in the T01.B BZ, which extends up to 70 m, and the high velocity, more typical of a blanket where liquid metal is also used as a coolant.

Mitigation strategies must be introduced to reduce the baseline loss in order to make this configuration feasible. Mean velocity could be reduced by merging adjacent poloidal sub-elements, thus reducing also the number of hairpin bends, but this solution could lead to a weakening of the blanket structure and be not very efficient due to the switch from a slotted channel ($a/b > 1$) to a quasi-square one ($a/b < 1$), which is characterized by larger pressure coefficient in eq. (13). On the other hand, the aspect ratio can be increased by merging adjacent channels in the toroidal direction by, for instance, envisioning three channels per sub-element. Even if this strategy could allow to reduce losses by 25%, it is unlikely that the extensive modifications required to structural elements would not results in damaging the blanket stability. Therefore, the only viable strategy seems to be the electrical decoupling of fluid and wall via FCI or insulating coatings.

Finally, coupling phenomena will likely be akin to those that will be observed in the case of quasi-radial flow (T01.A) thanks to flow path similarity between two configurations. Higher mean velocity and, thus, stronger leakage currents could lead to an increase in the harmful coupling side effects, especially for flow reversal regions.

8.3. Poloidal once-through flow (T02)

A very simple layout is adopted where the BZ is composed by straight rectangular ducts that, since they are aligned with poloidal direction, are only affected by the toroidal field. In general, the magnetic field is not uniform and a gradient is present among the back and front channels, where the field is strongest. However, the gradient is quite small (i.e.$\partial_x \tilde{B} \ll 1$) and is compensated by the longer length and larger size of the back channels. No complex hydraulic element is present and, assuming that the flow can be described by a local fully developed state to account for slowly varying cross-section and field intensity along the poloidal direction, the only 3D flow contribution to the pressure drop is from the flow around cooling pipes.

Typical FW channel is characterized by a toroidal and radial dimension, i.e. $2a \times 2b = 164 \times 147$ mm, whereas sub-channel flow rate is equal to $\Gamma_i = \Gamma_{OB}/32 = 0.512$ kg s^{-1}. It follows that $u_0 = 2.17$ mm s^{-1} and, for average FW field $B_t = 4.19$ T, $\nabla p_{FW} = 3.255$ kPa m^{-1}. It is straightforward to extend this argument to a back channel which size is only slightly larger in the radial direction, i.e. $2a \times 2b = 164 \times 167$ mm, so that $u_0 = 1.91$ mm s^{-1} and, for $B_t = 3.91$ T, $\nabla p_{BSS} = 2.450$ kPa m^{-1}. Linear length of the channel is calculated at $L_{FW} = 14.67$ m and $L_{BSS} = 16.94$ m, from which it is found the overall two-dimensional loss: $\Delta p_{FW,2D} = 47.74$ and $\Delta p_{BSS,2D} = 42.34$ kPa.

Cooling elements are composed by two nested U-pipes which refrigerate a four-channel radial array. Pressure loss due to 3D flow was estimated at 376.2 Pa per obstacle for the FW channel [9, 10]. Thermal considerations indicate that the vertical pitch between cooling elements must not exceed $p_v = 40$ mm, therefore $n = L_{FW}/p_v \approx 367$ must be foreseen to meet design requirements and $\Delta p_{FW,3D} = 138.1$ kPa. It is not easy to extrapolate the results of Ref. [9] to characterize the other T02 channels due to different pipe geometry, nevertheless is likely that $\Delta p_{BSS,3D} \leq \Delta p_{FW,3D}$ thanks to the lower blockage ratio.

The obstacle contribution has a fundamental impact on the BZ pressure drop estimate, since it constitutes $\approx 75\%$ of the FW channel loss. Even accounting for lower $\Delta p_{BSS,3D}$, imbalance calculated across front and back ducts should be small, i.e. less than $10 \div 20$ kPa including manifold contribution, and no significant overfeeding is expected from first-order effects.

Since the breeding zone is composed by an assembly of co-flowing quasi-square channels, it is relatively straightforward to devise how coupling phenomena will qualitatively affect the breeder flow by extrapolating from the results in Refs. [43, 44]. Coupling through side walls is going to be the dominant mechanism and will likely cause enhanced flow rate for front and back channels, together with dampened velocity in the central region. Secondary effects from coupling via Hartmann walls are going to shift a small portion of the flow rate toward the central channels in a toroidal row. Flow rearrangement due to coupling will

Table 23: T03 BZ channel equivalent cross section and fully developed flow pressure gradient, for channel labeling refers to Figure 7

	Pipes [31]	A (cm^2)	$\hat{A}$ (cm^2)	$\hat{A}/A$ (%)	u_0 ($mm\,s^{-1}$)	B_t (T)	∇p_{2D} ($kPa\,m^{-1}$)
Ia	2	274	271	99.0	3.85	3.91	5.052
IIa	3	241	237	98.2	4.41	3.91	5.783
IIb	6	241	233	96.4	4.49	4.19	6.750
Ib	17	241	217	89.9	4.82	4.19	7.241

probably cause a small rise (10÷15%) in the predicted pressure loss due to the combination of side wall (increase) and Hartmann wall (decrease) coupling [43].

8.4. Poloidal counter-flow (T03)

SP layout is shared between this one and previous configuration, as it is shown in Figure 7, whereas cooling system is modified to adopt vertical pipes. A variable number of cooling pipes is envisioned to refrigerate channels on the radial array going from $n = 17$ for the FW duct to just $n = 2$ for the back one [31]. The liquid metal flows downward at first on the blanket back and then rises in the front channels, therefore it is useful to consider an "external", composed by the front and back channels, and an "internal" flow path, composed by the central ducts, respectively labeled I and II in Figure 7. Since it is assumed that cooling pipes do not introduce additional losses, the pressure gradient can be computed from the effective cross-section available for the liquid metal flow, as detailed in Table 23, which is defined with the expression $\hat{A} = A - n \cdot \pi(d/2)^2$. Pipe diameter is taken as $d = 0.0135$ m and the flow rate is assumed to be evenly distributed, such that $\Gamma = 1.024\ kg\,s^{-1}$ for every one of the 16 BZ channels. Wall thickness is assumed to be uniform such that $c = 0.169$, a value which is representative of both Hartmann and side walls in the configuration.

If the downward and upward channel lengths are 14.667 and 16.94 m, the baseline pressure loss is calculated as

$$\Delta p_{\mathrm{I}} = \Delta p_{\mathrm{Ia}} + \Delta p_{\mathrm{Ib}} = 191.77\ \mathrm{kPa} \tag{20}$$

$$\Delta p_{\mathrm{II}} = \Delta p_{\mathrm{IIa}} + \Delta p_{\mathrm{IIb}} = 196.95\ \mathrm{kPa} \tag{21}$$

Downward and upward return channels are connected at the blanket bottom through two 90° bends and a radially oriented elbow channel which poloidal height is equal to the feeding duct width. Connection for external channel I is accompanied by a cross-section contraction, whereas there is no significant variation for the internal one. Both bends and contraction are perpendicular to toroidal field, which is equal to 4.87 T at blanket bottom, and their contribution is relatively small with the overall loss being dominated by the radial flow. Elbow loss is calculated at $\Delta p_{I,e} = 5.968$ and $\Delta p_{II,e} = 1.747$ kPa. Overall, no significant pressure imbalance is found between the two flow paths with a representative BZ loss $\Delta p \approx 198$ kPa, nearly more than 45% of the loss calculated for poloidal once-through flow in configuration T02.

Coupling phenomena are expected to follow the same pattern described for configuration T02 and can be extrapolated from Refs. [43, 44]. Notably, internal channels (IIa and IIb) are counter-flowing and coupled via the side walls, which will cause a jet promotion at the shared wall parallel to the magnetic field but no overall pressure loss modification [43]. On the other hand, co-flowing downward (Ia and IIa) and upward (Ib and IIb) channels are going to experience both Hartmann and side wall coupling in a similar fashion to what will be observed in configuration T02. As such, overall loss behavior is not expected to deviate much and a small increase (5÷10%) should be observed compared with uncoupled case

Finally, both downward channels and, in particular, the internal one (IIa) could be affected by buoyancy forces due to their considerable axial length. Likelihood of flow reversal should be carefully assessed for this configuration but it is probably high. Considering the internal channel ($a \times b = 82 \times 73.5$ mm), average volumetric heating is $Q = 0.6\ MW\,m^{-3}$ and, if $\Delta T = Qb^2/k$ with $k = 15.6\ W\,m\,K^{-1}$, it is found from Equation (6) that $Gr = 4.89 \times 10^9$. Moreover, from data collected in Table 23, $Re = 4.8 \times 10^3$ and $Ha = 7.5 \times 10^3$. Following the argument presented in Ref. [94], it is possible to define a reduced Grashof number r and shape parameter m

$$r = \sqrt{\frac{Gr}{HaRe(b/a)^2}} \tag{22}$$

$$m = b/L_{BSS} \tag{23}$$

For the internal downward channel, it is calculated that $r \approx 13$ and $m = 4.3 \times 10^{-3}$. According to Ref. [94], if $m \to 0$, then reverse flow occurs in the downward channel for $r > 1.6$. Intense flow reversal in the downward channels could be harmful due to inefficient PbLi circulation and potential tritium accumulation. However, since the interested channels are relatively far away from the FW, where the bulk of breeding occurs, the impact of flow reversal on permeation toward the coolant could be minor.

9. Conclusions

The influence of PbLi loop layout on MHD losses for the WCLL blanket outboard segment has been assessed through a system-level methodology supported, wherever possible, by the results of direct simulation activities. Four alternative configurations were considered featuring different layouts for the connection pipes (feeding and draining), distribution components, and breeding zone.

The analysis highlighted that connection pipe layout and reactor integration constraints on these components are the key factors in determining the overall MHD pressure drop in the PbLi loop. This condition is verified, in particular, for WCLL T01.A where BZ losses are negligible thanks to the very low PbLi mean velocity (≈0.2 $mm\,s^{-1}$). To minimize the MHD loss and simplify the

magneto-hydraulic path within the blanket segment, an integration scheme featuring feeding pipe integrated in the lower port and draining pipe in the upper port seems to be the best solution, especially if sufficiently large pipes (i.e. DN$\geq$150) can be hosted in the former. Other integration solutions increase the pressure loss figure by a substantial amount and could benefit by introducing electrical decoupling elements (i.e. FCI) in the blanket design.

Manifold losses appear to be a second order effect when accounting for the whole PbLi loop, but are likely affected by a wider uncertainty due to the complex layout and poor characterization. More accurate understanding of 3D MHD manifold flows is severely needed to improve the current estimate and it is the only way to assess the actual flow distribution in the blanket segment. This statement is particularly true for the spinal manifold layout which features a combination of flow around obstacles, coupling phenomena, and compact geometry.

Rearrangement of SP layout to re-route PbLi toward a mostly poloidal flow (i.e. T02 and T03) showed significant potential in pressure loss reduction and simplified flow distribution through plenum or honeycomb manifold concepts. However, it is not clear if and how much the segment mechanical stability will be affected by adopting these configurations. Main issues have been highlighted about the bottom cap design, manifold and BZ refrigeration, and wide flow reversals in downward channels.

To provide a more complete picture of the MHD loss in PbLi loop, the system-level estimate should be extended to cover also the inboard segment, where a substantially higher figure is expected, even if flow rate is lower, due to larger magnetic field intensity (i.e. 5$\div$9 T). A similar analysis will be performed once the WCLL inboard design reach a sufficient maturity to allow for enough geometrical data and accurate boundary conditions.

Acknowledgements

This work has been carried out within the framework of the EUROfusion Consortium and has received funding from the Euratom research and training programme 2014-2018 and 2019-2020 under grant agreement No 633053. The views and opinions expressed herein do not necessarily reflect those of the European Commission.

References

[1] M. Abdou, N. B. Morley, S. Smolentsev, A. Ying, S. Malang, A. Rowcliffe, M. Ulrickson, Blanket/first wall challenges and required R&D on the pathway to DEMO, Fusion Engineering and Design 100 (2015) 2–43. Doi: 10.1016/j.fusengdes.2015.07.021.

[2] S. Smolentsev, R. Moreau, L. Bühler, C. Mistrangelo, MHD thermofluid issues of liquid-metal blankets: phenomena and advances, Fusion Engineering and Design 85 (2010) 1196–1205. Doi: 10.1016/j.fusengdes.2010.02.038.

[3] M. Utili, S. Bassini, L. Boccaccini, L. Bühler, F. Cismondi, A. Del Nevo, M. Eboli, F. Di Fonzo, T. Hernandez, S. Wulf, et al., Status of Pb-16Li technologies for European DEMO fusion reactor, Fusion Engineering and Design (2019). Doi: 10.1016/j.fusengdes.2019.04.083.

[4] A. Del Nevo, P. Arena, G. Caruso, P. Chiovaro, P. Di Maio, M. Eboli, F. Edemetti, N. Forgione, R. Forte, A. Froio, et al., Recent progress in developing a feasible and integrated conceptual design of the WCLL BB in EUROfusion project, Fusion Engineering and Design (2019). Doi: 10.1016/j.fusengdes.2019.03.040.

[5] A. Tassone, G. Caruso, A. Del Nevo, I. Di Piazza, CFD simulation of the magnetohydrodynamic flow inside the WCLL breeding blanket module, Fusion Engineering and Design 124 (2017) 705–709. doi:10.1016/j.fusengdes.2017.05.098.

[6] A. Tassone, M. Nobili, G. Caruso, Magnetohydrodynamic flow and heat transfer around a heated cylinder of arbitrary conductivity, in: Journal of Physics: Conference Series, volume 923, IOP Publishing, 2017, p. 012024. doi:10.1088/1742-6596/923/1/012024.

[7] A. Tassone, M. Nobili, G. Caruso, Numerical study of the MHD flow around a bounded heating cylinder: Heat transfer and pressure drops, International Communications in Heat and Mass Transfer 91 (2018) 165–175. Doi: 10.1016/j.icheatmasstransfer.2017.12.010.

[8] A. Tassone, L. Gramiccia, G. Caruso, Three-dimensional mhd flow and heat transfer in a channel with internal obstacle, International Journal of Heat and Technology 36 (2018) 1367–1377. Doi: 10.18280/ijht.360428.

[9] A. Tassone, G. Caruso, F. Giannetti, A. Del Nevo, MHD mixed convection flow in the WCLL: Heat transfer analysis and cooling system optimization, Fusion Engineering and Design (2019). Doi: 10.1016/j.fusengdes.2019.01.087.

[10] A. Tassone, Study on liquid metal magnetohydrodynamic flows and numerical application to a water-cooled blanket for fusion reactors, PhD thesis, Sapienza University of Rome, March 2019. Available online at: https://iris.uniroma1.it/retrieve/handle/11573/1243658/1054590/Tesi_dottorato_Tassone.pdf.

[11] J. Reimann, G. Benamati, R. Moreau, Report of the Working Group MHD for the Blanket Concept Selection Exercise (BCSE, Forschungszentrum Karlsruhe, 1995. Tech. Rep. FZKA 5652.

[12] L. Bühler, P. Norajitra, Magnetohydrodynamic flow in the dual coolant blanket, Forschungszentrum Karlsruhe, 2003. Tech. Rep. FZKA 6802.

[13] D. Rapisarda, I. Palermo, M. Gonzalez, F. Martin-Fuertes, C. Moreno, A. Ibarra, I. Fernandez, E. M. de les Valls, Overview of DCLL research activities in the EU/Spain, in: 2015 IEEE 26th Symposium on Fusion Engineering (SOFE), IEEE, 2015, pp. 1–8.

[14] S. Smolentsev, N. B. Morley, C. Wong, M. Abdou, MHD and heat transfer considerations for the US DCLL blanket for DEMO and ITER TBM, Fusion Engineering and Design 83 (2008) 1788–1791. Doi: 10.1016/j.fusengdes.2008.04.002.

[15] S. Smolentsev, C. Wong, S. Malang, M. Dagher, M. Abdou, MHD considerations for the DCLL inboard blanket and access ducts, Fusion Engineering and Design 85 (2010) 1007–1011. Doi: 10.1016/j.fusengdes.2009.12.005.

[16] P. K. Swain, P. Koli, S. Ghorui, P. Mukherjee, A. V. Deshpande, Thermofluid MHD studies in a model of Indian LLCB TBM at high magnetic field relevant to ITER, Fusion Engineering and Design (2019). Under review.

[17] M. J. Wolfendale, M. J. Bluck, A coupled systems code-CFD MHD solver for fusion blanket design, Fusion Engineering and Design 98 (2015) 1902–1906. doi:10.1016/j.fusengdes.2015.04.025.

[18] C. Mistrangelo, L. Buhler, MHD mock-up experiments for studying pressure distribution in a helium-cooled liquid-metal blanket, IEEE Transactions on Plasma Science 38 (2010) 254–258. Doi: 10.1109/TPS.2009.2036261.

[19] C. Mistrangelo, L. Bühler, H.-J. Brinkmann, Experimental investigation of MHD pressure losses in a mock-up of a liquid metal blanket, Nuclear Fusion 58 (2018) 036012. Doi: 10.1088/1741-4326/aaa133.

[20] G. Federici, C. Bachmann, L. Barucca, W. Biel, L. Boccaccini, R. Brown, C. Bustreo, S. Ciattaglia, F. Cismondi, M. Coleman, et al., DEMO design activity in Europe: Progress and updates, Fusion Engineering and Design (2018). Doi: 10.1016/j.fusengdes.2018.04.001.

[21] G. Federici, L. Boccaccini, F. Cismondi, M. Gasparotto, Y. Poitevin, I. Ricapito, An overview of the EU breeding blanket design strategy as an integral part of the DEMO design effort, Fusion Engineering and Design 141 (2019) 30–42. Doi: 10.1016/j.fusengdes.2019.01.141.

[22] A. Del Nevo, E. Martelli, P. Agostini, P. Arena, G. Bongiovì, G. Caruso, G. Di Gironimo, P. Di Maio, M. Eboli, R. Giammusso, et al., WCLL breeding blanket design and integration for 2015: status and perspectives, Fusion Engineering and Design (2017). URL: 10.1016/j.fusengdes.2017.03.020.

[23] E. Martelli, A. Del Nevo, P. Arena, G. Bongiovì, G. Caruso, P. Di Maio, M. Eboli, G. Mariano, R. Marinari, F. Moro, et al., Advancements in DEMO WCLL breeding blanket design and integration, International Journal of Energy Research 42 (2018) 27–52. Doi: 10.1002/er.3750.

[24] A. Tassone, A. Del Nevo, P. Arena, G. Bongiovì, G. Caruso, P. A. di Maio, G. di Gironimo, M. Eboli, N. Forgione, R. Forte, et al., Recent progress in the WCLL breeding blanket design for the DEMO fusion reactor, IEEE Transactions on Plasma Science 46 (2018) 1446–1457. Doi: 10.1109/TPS.2017.2786046.

[25] M. Utili, A. Tincani, D. Martelli, C. Schweier, WPBB-DEL-BB-5.1.1-T001-D003, EFDA D 2MN9BR, Conceptual Design of WCLL/HCLL PbLi–Loops with Auxiliaries, Eurofusion, 2017. Available online for EUROfusion members at https://idm.eurofusion.org/?uid=2MQM7L.

[26] M. D'Onorio, F. Giannetti, G. Caruso, M. T. Porfiri, In-box LOCA accident analysis for the European DEMO water-cooled reactor, Fusion Engineering and Design (2019). Doi: 10.1016/j.fusengdes.2019.01.066.

[27] F. Urgorri, S. Smolentsev, I. Fernández-Berceruelo, D. Rapisarda, I. Palermo, A. Ibarra, Magnetohydrodynamic and thermal analysis of PbLi flows in poloidal channels with flow channel insert for the EU-DCLL blanket, Nuclear Fusion 58 (2018) 106001. Doi: 10.1088/1741-4326/aad299.

[28] P. A. Davidson, An introduction to magnetohydrodynamics, volume 25, Cambridge university press, 2001.

[29] U. Müller, L. Bühler, Magnetofluiddynamics in channels and containers, Springer Science & Business Media, 2013.

[30] R. Mozzillo, A. Del Nevo, E. Martelli, G. Di Gironimo, Alternative design of DEMO Water Cooled Lithium Lead internal structure, Fusion Engineering and Design (2019). Doi: 10.1016/j.fusengdes.2019.02.001.

[31] F. Edemetti, E. Martelli, A. Tassone, G. Caruso, A. Del Nevo, DEMO WCLL breeding zone cooling system design: Analysis and discussion, Fusion Engineering and Design (2019). Doi: 10.1016/j.fusengdes.2019.04.063.

[32] E. Martelli, G. Caruso, F. Giannetti, A. Del Nevo, Thermo-hydraulic analysis of EU DEMO WCLL breeding blanket, Fusion Engineering and Design 130 (2018) 48–55. Doi: 10.1016/j.fusengdes.2018.03.030.

[33] P. Di Maio, P. Arena, G. Bongiovì, I. Catanzaro, A. Del Nevo, R. Forte, On the effect of stiffening plates configuration on the DEMO Water Cooled Lithium Lead Breeding Blanket module thermo-mechanical behaviour, Fusion Engineering and Design (2019). Doi: 10.1016/j.fusengdes.2019.03.163.

[34] R. Wenninger, et al., EFDA D 2MUW9R, DEMO1 Reference Design - 2017 April ("EU DEMO1 2017") - SOF and EOF equilibria - v1.0, Eurofusion, 2018. Available online for EUROfusion members at https://idm.euro-fusion.org/?uid=2MUW9R.

[35] B. Schulz, Thermophysical properties of the Li (17) Pb (83) alloy, Fusion Engineering and Design 14 (1991) 199–205. Doi: 10.1016/0920-3796(91)90002-8.

[36] K. Mergia, N. Boukos, Structural, thermal, electrical and magnetic properties of Eurofer 97 steel, Journal of Nuclear Materials 373 (2008) 1–8. Doi: 10.1016/j.jnucmat.2007.03.267.

[37] AFCEN, RCC-MRx: Design and Construction Rules for Mechanical Components in high-temperature structures, experimental reactors and fusion reactors, Standard, 2015.

[38] L. Bühler, Three-dimensional liquid metal flows in strong magnetic fields, Forschungszentrum Karlsruhe, 2008. Tech. Rep. FZKA 7412.

[39] H. Madarame, K. Taghavi, M. Tillack, The influence of leakage currents on MHD pressure drop, Fusion Technology 8 (1985) 264–269. Doi: 10.13182/FST85-A40055.

[40] T. Q. Hua, B. F. Picologlou, Magnetohydrodynamic flow in a manifold and multiple rectangular coolant ducts of self-cooled blankets, Fusion Technology 19 (1991) 102–112. Doi: 10.13182/FST91-A29320.

[41] R. Stieglitz, S. Molokov, Experimental study of magnetohydrodynamic flows in electrically coupled bends, Journal of Fluid Mechanics 343 (1997) 1–28. Doi: 10.1017/S0022112097005788.

[42] C. Mistrangelo, L. Bühler, Electric flow coupling in the HCLL blanket concept, Fusion Engineering and Design 83 (2008) 1232–1237. Doi: 10.1016/j.fusengdes.2008.07.004.

[43] X. Zhang, C. Pan, Z. Xu, Investigation of coupling mhd rectangular ducts flows based on a fully developed modeling, IEEE Transactions on Plasma Science 42 (2014) 1764–1769. Doi: 10.1109/TPS.2014.2322071.

[44] M. J. Bluck, M. J. Wolfendale, An analytical solution to electromagnetically coupled duct flow in MHD, Journal of Fluid Mechanics 771 (2015) 595–623. Doi: 10.1017/jfm.2015.202.

[45] C. Mistrangelo, L. Bühler, Electro-magnetic flow coupling for liquid metal blanket applications, Fusion Engineering and Design 109 (2016) 1452–1457. Doi: 10.1016/j.fusengdes.2015.11.052.

[46] I. R. Kirillov, C. B. Reed, L. Barleon, K. Miyazaki, Present understanding of MHD and heat transfer phenomena for liquid metal blankets, Fusion engineering and design 27 (1995) 553–569. Doi: 10.1016/0920-3796(95)90171-X.

[47] K. Miyazaki, S. Inoue, N. Yamaoka, T. Horiba, K. Yokomizo, Magneto-hydro-dynamic pressure drop of lithium flow in rectangular ducts, Fusion Technology 10 (1986) 830–836. Doi: 10.13182/FST10-830.

[48] K. Miyazaki, S. Kotake, N. Yamaoka, S. Inoue, Y. Fujii-E, MHD pressure drop of NaK flow in stainless steel pipe, Nuclear Technology-Fusion 4 (1983) 447–452. Doi: 10.13182/FST4-2P2-447.

[49] T. Hua, J. Walker, B. Picologlou, C. Reed, Three-dimensional magnetohydrodynamic flows in rectangular ducts of liquid-metal-cooled blankets, Fusion Technology 14 (1988) 1389–1398.

[50] I. A. Evtushenko, I. R. Kirillov, C. B. Reed, Mhd-flow in slotted channels with conducting walls, Fusion engineering and design 27 (1995) 627–633. Doi: 10.1016/0920-3796(95)90177-9.

[51] Z. Xu, J. Chen, J. Qian, W. Jiang, C. Pan, W. Li, Magnetohydrodynamic pressure drop in a quickly changing magnetic field, Fusion engineering and design 27 (1995) 678–681. Doi: 10.1016/0920-3796(95)90183-3.

[52] Z. Xu, C. Pan, W. Wei, X. Chen, Y. Zhang, W. Li, Experimental investigation and theoretical analysis of two-dimensional magnetohydrodynamic effects in a rectangular duct, Fusion Technology 36 (1999) 47–51. Doi: 10.13182/FST99-A90.

[53] F.-C. Li, D. Sutevski, S. Smolentsev, M. Abdou, Experimental and numerical studies of pressure drop in PbLi flows in a circular duct under non-uniform transverse magnetic field, Fusion Engineering and Design 88 (2013) 3060–3071. Doi: 10.1016/j.fusengdes.2013.08.006.

[54] Z. Meng, Z. Zhu, J. He, M. Ni, Experimental studies of MHD pressure drop of PbLi flow in rectangular pipes under uniform magnetic field, Journal of Fusion Energy 34 (2015) 759–764. Doi: 10.1007/s10894-015-9848-0.

[55] S. Smolentsev, C. Courtessole, M. Abdou, S. Sharafat, S. Sahu, T. Sketchley, Numerical modeling of first experiments on PbLi MHD flows in a rectangular duct with foam-based SiC flow channel insert, Fusion Engineering and Design 108 (2016) 7–20. Doi: 10.1016/j.fusengdes.2016.04.035.

[56] L. Bühler, H.-J. Brinkmann, C. Koehly, Experimental study of liquid metal magnetohydrodynamic flows near gaps between flow channel inserts, Fusion Engineering and Design (2018). Doi:

10.1016/j.fusengdes.2018.11.034.

[57] M. Tillack, A. Ying, H. Hashizume, The effect of magnetic field alignment on heat transfer in liquid metal blanket channels, in: IEEE Thirteenth Symposium on Fusion Engineering, IEEE, 1989, pp. 376–379. Doi: 10.1109/FUSION.1989.102243.

[58] L. Bühler, Magnetohydrodynamic flows in arbitrary geometries in strong, nonuniform magnetic fields—a numerical code for the design of fusion reactor blankets, Fusion Technology 27 (1994) 3–24.

[59] T. Q. Hua, J. S. Walker, MHD flow in rectangular ducts with inclined non-uniform transverse magnetic field, Fusion engineering and design 27 (1995) 703–710. Doi: 10.1016/0920-3796(95)90186-8.

[60] R. J. Holroyd, An experimental study of the effects of wall conductivity, non-uniform magnetic fields and variable area ducts on liquid metal flows at high Hartmann number. Part 2. Ducts with conducting walls, Journal of Fluid Mechanics 96 (1980) 355–374. Doi: 10.1017/S0022112080002169.

[61] L. Barleon, L. Bühler, K. Mack, R. Stieglitz, B. Picologlou, T. Hua, C. Reed, Liquid metal flow through a right angle bend in a strong magnetic field, Fusion Technology 21 (1992) 2197–2203. Doi: 10.13182/FST92-A30045.

[62] J. Reimann, S. Molokov, I. Platnieks, E. Platacis, MHD-flow in multichannel U-bends: screening experiments and theoretical analysis, in: Fusion Technology 1992, Elsevier, 1993, pp. 1454–1458. Doi: 10.1016/B978-0-444-89995-8.50285-X.

[63] R. Stieglitz, L. Barleon, L. Bühler, S. Molokov, Magnetohydrodynamic flow in a right-angle bend in a strong magnetic field, Journal of Fluid Mechanics 326 (1996) 91–123. Doi: 10.1017/S0022112096008257.

[64] P. Swain, P. Satyamurthy, R. Bhattacharyay, A. Patel, A. Shishko, E. Platacis, A. Ziks, S. Ivanov, A. Despande, 3D MHD lead–lithium liquid metal flow analysis and experiments in a test-section of multiple rectangular bends at moderate to high Hartmann numbers, Fusion Engineering and Design 88 (2013) 2848–2859. Doi: 10.1016/j.fusengdes.2013.05.048.

[65] T. Moon, J. Walker, Liquid metal flow in a large-radius elbow with a uniform magnetic fluid, Journal de Mecanique Theorique et Appliquee 7 (1988).

[66] T. Moon, J. Walker, Liquid metal flow through a sharp elbow in the plane of a strong magnetic field, Journal of Fluid Mechanics 213 (1990) 397–418. Doi: 10.1017/S0022112090002373.

[67] T. Moon, T. Hua, J. Walker, Liquid-metal flow in a backward elbow in the plane of a strong magnetic field, Journal of fluid mechanics 227 (1991) 273–292. Doi: 10.1017/S0022112091000113.

[68] S. Molokov, L. Bühler, Liquid metal flow in a U-bend in a strong uniform magnetic field, Journal of Fluid Mechanics 267 (1994) 325–352. Doi: 10.1017/S0022112094001205.

[69] S. Molokov, Liquid metal flows in manifolds and expansions of insulating rectangular ducts in the plane perpendicular to a strong magnetic field, Forschungszentrum Karlsruhe, 1994. Tech. Rep. FZKA 5272.

[70] Q. He, J. Feng, H. Chen, Numerical analysis and optimization of 3D magnetohydrodynamic flows in rectangular U-bend, Fusion Engineering and Design 109 (2016) 1313–1317. Doi: 10.1016/j.fusengdes.2015.12.036.

[71] J. Hunt, S. Leibovich, Magnetohydrodynamic flow in channels of variable cross-section with strong transverse magnetic fields, Journal of Fluid Mechanics 28 (1967) 241–260. Doi: 10.1017/S0022112067002046.

[72] J. Hunt, G. Ludford, Three-dimensional MHD duct flows with strong transverse magnetic fields. Part 1. Obstacles in a constant area channel, Journal of Fluid Mechanics 33 (1968) 693–714. Doi: 10.1017/S002211206800162X.

[73] J. Walker, G. Ludford, J. Hunt, Three-dimensional mhd duct flows with strong transverse magnetic fields. part 2. variable-area rectangular ducts with conducting sides, Journal of Fluid Mechanics 46 (1971) 657–684. Doi: 10.1017/S0022112071000776.

[74] C. Mistrangelo, Three-dimensional MHD flow in sudden expansions, Forschungszentrum Karlsruhe, 2006. Tech. Rep. FZKA 7201.

[75] C. N. Kim, A liquid metal magnetohydrodynamic duct flow with sudden contraction in a direction perpendicular to a magnetic field, Computers & Fluids 108 (2015) 156–167. Doi: 10.1016/j.compfluid.2014.12.001.

[76] J. Feng, Q. He, H. Chen, M. Ye, Numerical investigation of magnetohydrodynamic flow through sudden expansion pipes in liquid metal blankets, Fusion Engineering and Design 109 (2016) 1360–1364. Doi: 10.1017/S0022112071000776.

[77] V. Dousset, A. Pothérat, Numerical simulations of a cylinder wake under a strong axial magnetic field, Physics of Fluids 20 (2008) 017104. Doi: 10.1063/1.2831153.

[78] Z. E. Kalis, A. Tsinober, A. Shtern, E. Shcherbinin, Flow of conducting fluid past circular cylinder in the presence of transverse magnetic field, Magnetohydrodynamics 1 (1965) 18–28.

[79] A. Tsinober, P. Shtern, Experimental investigation of the pressure distribution for constrained MHD flow past cylinders, Magnetohydrodynamics 9 (1973) 12–18.

[80] G. Mutschke, G. Gerbeth, V. Shatrov, A. Tomboulides, The scenario of three-dimensional instabilities of the cylinder wake in an external magnetic field: A linear stability analysis, Physics of Fluids 13 (2001) 723–734. Doi: 10.1063/1.1344895.

[81] W. K. Hussam, M. C. Thompson, G. J. Sheard, Dynamics and heat transfer in a quasi-two-dimensional MHD flow past a circular cylinder in a duct at high Hartmann number, International Journal of Heat and Mass Transfer 54 (2011) 1091–1100. Doi: 10.1016/j.ijheatmasstransfer.2010.11.013.

[82] O. Andreev, Y. B. Kolesnikov, Experimental flow around a conducting cylinder in an axial homogeneous magnetic field, Magnetohydrodynamics 34 (1998) 286–293.

[83] M. Frank, L. Barleon, U. Müller, Visual analysis of two-dimensional magnetohydrodynamics, Physics of fluids 13 (2001) 2287–2295. Doi: 10.1063/1.1383785.

[84] N. Kanaris, X. Albets, D. Grigoriadis, S. Kassinos, Three-dimensional numerical simulations of magnetohydrodynamic flow around a confined circular cylinder under low, moderate, and strong magnetic fields, Physics of Fluids 25 (2013) 074102. Doi: 10.1063/1.4811398.

[85] J. Aubert, G. Aiello, N. Jonquères, A. L. Puma, A. Morin, G. Rampal, Development of the water cooled lithium lead blanket for DEMO, Fusion Engineering and Design 89 (2014) 1386–1391. Doi: 10.1016/j.fusengdes.2014.01.061.

[86] L. Bühler, C. Mistrangelo, MHD flow and heat transfer in model geometries for WCLL blankets, Fusion Engineering and Design 124 (2017) 919–923. Doi: 10.1016/j.fusengdes.2017.01.014.

[87] F. R. Urgorri, I. Fernández-Berceruelo, A. Tassone, F. Edementti, E. Martelli, A. Del Nevo, D. Rapisarda, A. Ibarra, MHD and heat transfer analyses in PbLi radial channels for the EUROfusion WCLL breeding blanket, in: Proceedings of 11th PAMIR International Conference - Fundamental and Applied MHD, July 1 – 5, 2019, Reims, France, 2019, pp. 1–5.

[88] L. Bühler, C. Mistrangelo, Effects of radial variation of the magnetic field on the pressure distribution in the european liquid-metal blanket concept, Fusion Science and Technology 60 (2011) 257–263. Doi: 10.13182/FST11-A12362.

[89] C. Koehly, L. Bühler, Fabrication issues of sandwich-like flow inserts for circular pipes, Fusion Science and Technology 72 (2017) 660–666. Doi: 10.1080/15361055.2017.1350477.

[90] F. Cismondi, L. Boccaccini, G. Aiello, J. Aubert, C. Bachmann, T. Barrett, L. Barucca, E. Bubelis, S. Ciattaglia, A. Del Nevo, et al., Progress in EU Breeding Blanket design and integration, Fusion Engineering and Design 136 (2018) 782–792. doi:10.1016/j.fusengdes.2018.04.009.

[91] L. Bühler, C. Mistrangelo, Pressure drop and velocity changes in MHD pipe flows due to a local interruption of the insulation, Fusion Engineering and Design 127 (2018) 185–191. Doi: 10.1016/j.fusengdes.2018.01.010.

[92] L. Bühler, C. Mistrangelo, Theoretical studies of mhd flows in support to hcll design activities, Fusion Engineering and Design 109 (2016) 1609–1613. Doi: 10.1016/j.fusengdes.2015.11.010.

[93] C. Mistrangelo, L. Bühler, Determination of multichannel MHD

velocity profiles from wall-potential measurements and numerical simulations, Fusion Engineering and Design 130 (2018) 137–141. Doi: 10.1016/j.fusengdes.2018.03.041.

[94] S. Smolentsev, R. Moreau, M. Abdou, Characterization of key magnetohydrodynamic phenomena in PbLi flows for the US DCLL blanket, Fusion Engineering and Design 83 (2008) 771–783. Doi: 10.1016/j.fusengdes.2008.07.023.